

ABSTRACT

WINFREY, A. LEIGH. Nanocrystalline Diamond Deposition for Friction Applications. (Under the direction of Dr. Jack E. Rowe and Dr. Robert J. Nemanich).

The structure and morphology of nanocrystalline diamond films, grown on single side polished silicon (100) wafers by microwave plasma assisted chemical vapor deposition in Ar-H-CH₄ plasma, with varying hydrogen concentrations, were analyzed and examined using Raman spectroscopy, scanning electron microscopy, atomic force microscopy, near edge x-ray absorption fine structure spectroscopy, and x-ray diffraction. Visible Raman spectra, XRD data, and NEXAFS spectra exhibit fingerprints for NCD films. Broad bands at 1350 and 1520-1580 cm⁻¹ with shoulders at 1100-1150 cm⁻¹ and 1430-1470 cm⁻¹ and a shoulder at 1150cm⁻¹ are evident in the Raman spectra. The XRD analysis reveals small grain sizes, 5 to 10 nm. The NEXAFS spectra discussed in this thesis are similar to characteristic NCD spectra in the literature and show distinct diamond character. Friction performance was studied using Pin-on-Disk and Reciprocating sliding tribometry with sapphire counterfaces. Tribological performance of nanocrystalline diamond coatings was not influenced by coating roughness over the range studied (20 – 60 nm); however, the coating performance was influenced by coating chemistry. High friction run-in was minimized and a low final friction coefficient <0.05 was measured. These coatings exhibited good wear resistance for sliding against sapphire hemispheres. Their performance was correlated to their properties and structure, which were also studied. Plasma modeling and optical emission spectroscopy revealed plasma parameters, electron plasma temperature and number density, consistent with published results.

Nanocrystalline Diamond Deposition for Friction Applications

by
A. Leigh Winfrey

A thesis submitted to the Graduate Faculty of
North Carolina State University
in partial fulfillment of the
requirements for the Degree of
Master of Science

Physics

Raleigh, North Carolina

2007

APPROVED BY:

J. E. Rowe
Chair of Advisory Committee

R. J. Nemanich
Co-Chair

O.E. Hankins
Minor Representative

DEDICATION

To my parents.

BIOGRAPHY

Leigh Winfrey was born in Texas and raised in North Carolina. She was educated in Greensboro and Charlotte, North Carolina. She attended the University of North Carolina at Charlotte and graduated in 2003 with a Bachelors of Science in Physics and 2004 with a Bachelors of Arts in Chemistry and Mathematics. After completing her undergraduate degrees, Leigh began her graduate work at North Carolina State University in 2004.

ACKNOWLEDGEMENTS

I would first like to acknowledge my parents, Christa and J.D.; I would not have arrived at this point without their unwavering love and support. Additionally, I would like to thank all my “old” friends for their support and encouragement through out my early education and college, specifically: Jessica Johnson, Bridget Fitzgerald, Aja Andreu, Heather Hall, GF Stout, and Russell Henderson. Since beginning graduate school, I have also become friends with a group of wonderful people: you know who you are! However, I would like to acknowledge Mary Bridget Kustusch, Jeff Mullen, and Rich Chromik in particular, without them this work would not have been possible (nor half as much fun).

I would next like to thank Dr. Robert Nemanich and Dr. Jack Rowe for their direction and support during this research, my thanks also to Dr. Orlando Hankins for serving as my minor representative and for his discussions on plasmas and optical emission spectroscopy. Also, my thanks to past and present members of the Surface Science Lab, especially Jacob Garguillo, Franz Köck, and Matt Bruckman. Other collaborators and advisors that I would like to acknowledge are Dr. Kathryn Wahl, Dr. Albert Young, Elijah Martin, and Dr. Mohammed Bourham.

TABLE OF CONTENTS

	Page
LIST OF TABLES	vi
LIST OF FIGURES	vii
1. Introduction	1
2. Deposition of NCD Coatings	10
2.1 Chemical Vapor Deposition.....	10
2.1.1 Microwave Discharges.....	11
2.1.2 NCD Deposition Technique.....	18
3. Materials Characterization and Analysis of NCD Coatings	21
3.1 Surface Science: AFM and SEM	21
3.2 Raman Spectroscopy.....	24
3.3 X-Ray Diffraction	25
3.4 Near Edge X-ray Absorption Fine Structure	29
3.5 Transmission Electron Microscopy	31
3.6 Nuclear Scattering for Elemental Analysis.....	33
3.7 Summary of Characterization and Analysis	37
4. Plasma Characterization by Optical Emission Spectroscopy	39
4.1 Electron Plasma Temperature	39
4.2 Electron Plasma Number Density	40
4.3 Experimental Setup for Spectroscopic Measurements	41
4.4 Experimental Measurements.....	44
4.5 Methane Plasma Description and Model	44
4.6 Summary of Plasma Characteristics	51
5. Tribology Studies of Nanocrystalline Diamond Coatings	53
5.1 Reciprocating Sliding Tribology of NCD Coatings.....	53
5.1.1 Experimental Setup and Measurements.....	53
5.1.2 <i>Ex Situ</i> Analysis – Wear Tracks and Transfer Films	55
5.1.3 <i>In Situ</i> Observations.....	59
5.2 Pin-on-Disk Tribology	61
5.2.1 Experimental Setup and Measurements.....	61
5.2.2 Pin on Disk Friction Behavior and Performance	62
6. Discussion	66
6.1 Tribology and Materials Characteristics	66
6.2 Plasma and Materials Characteristics	73

7. Conclusions and Future Work.....	75
8. References.....	78

LIST OF TABLES

	Page
<i>Table 3.1 Characteristics of the nanocrystalline diamond coatings determined from AFM, x-ray diffraction, and NEXAFS. The intensity of the graphite peak varied from sample to sample and is normalized to the sum of diamond (220) and (111) peak intensities.....</i>	23
<i>Table 3.2 H90 Analysis and Elemental Content.....</i>	36
<i>Table 3.3 H36 Analysis and Elemental Content.....</i>	36
<i>Table 3.4 H0 Analysis and Elemental Content.....</i>	36
<i>Table 3.5 Error and Tolerance in Scattering Analysis and Elemental Content.....</i>	36
<i>Table 4.1 Second order reaction rate coefficients for methane plasma; (a) indicates the dominant reaction(s), and (b) similar reaction rates.....</i>	47
<i>Table 4.2 Percentage of each reaction in the methane plasma modeled in this thesis.....</i>	48
<i>Table 5.1 Results for tribological performance of the nanocrystalline diamond coatings.....</i>	55
<i>Table 5.2 Cycles to run-in for Pin-on-Disk tribometry.....</i>	62

LIST OF FIGURES

	Page
<i>Figure 1.1 Schematic showing the differences in nucleation and growth of (a) microcrystalline diamond with large growth domains, (b) nanocrystalline diamond with smaller domains and relatively thick grain boundaries, and (c) ultra-nanocrystalline diamond films with minimum achievable grain size and grain boundary thickness.....</i>	6
<i>Figure 2.1 (a) Low aspect ratio microwave discharge; the heating zone is close to the cavity exit at the interface with the discharge chamber. (b) Coupling microwave source to waveguide and plasma via stub tuners for maximum forward and minimum reflected power, plasma takes a conical shape as it emerges from the cavity into the reaction chamber. (c) High aspect ratio microwave discharge, the heating zone is inside the cavity and may be close to the launching window. (d) High aspect ratio single cavity discharge, similar to that used in this thesis, plasma forms a spherical shape on top of the substrate</i>	12
<i>Figure 2.2 Schematic of the microwave PECVD CVD system used for the films in this thesis. In addition to deposition on silicone wafers, ¼ inch diameter sapphire hemispheres were employed on for self mated friction experiments.....</i>	20
<i>Figure 3.1 SEM and AFM images films grown in different plasma environments. H# refers to the percent of H2 in the total gas flow.....</i>	22
<i>Figure 3.2 Raman spectra for samples H0, H8.5 and H36 obtained with 514 nm excitation.....</i>	24
<i>Figure 3.3 X-ray diffraction scans showing diamond (111), (220), and (311) peaks for samples H0, H8.5, and H36</i>	27
<i>Figure 3.4 NEXAFS scans for samples H0, H8.5, H10, H14, H36 and a graphite standard used in data reduction. The scans show the diamond exciton at ~288.5 eV and the diamond 2nd band gap at ~303 eV</i>	30

Figure 3.5	<i>H36 a representative TEM sample showing two in phase diamond grains, highlighted blue and red.....</i>	32
Figure 3.6	<i>A TEM sample showing sp^2 (red), sp^3 (blue), and mixed (green) regions. The surface is on the right of the image.....</i>	33
Figure 3.7	<i>A schematic of the RBS/HFS experimental set up</i>	34
Figure 3.8	<i>Ternary diagram showing different carbon coatings and their $sp^3/sp^2/H$ content. The films discussed in this thesis fall in the purple oval marked NCD.....</i>	38
Figure 4.1	<i>Simplified diagram showing the experimental arrangement for emission spectroscopy, fiber optics pointing close to the surface of the substrate.....</i>	42
Figure 4.2	<i>Variation of reaction rate constants as a function of electron plasma temperature</i>	46
Figure 4.3	<i>CVD plasma temperature related to gas mixture. H2 90 indicates hydrogen makes up 90 % of the plasma. In all cases except H2 and H2 98 methane is 10% of the plasma, hydrogen is as indicated and argon makes up the remaining part of the mixture.....</i>	49
Figure 4.4	<i>Spectrum of a plasma with 10% methane, 54% argon, and 36% hydrogen</i>	50
Figure 4.5	<i>Visible spectrum of a plasma with 10% methane, 54% argon, and 36% hydrogen.....</i>	51
Figure 5.1	<i>AFM images of coating H8.5: (a) as prepared coating and wear tracks at (b) 1 cycle, (c) 100 cycles and (d) 1500 cycles</i>	55
Figure 5.2	<i>EDS data for (a) wear tracks on coating H0 and H36, and for (b) endpatches on H0 and H36 (c) SEM image of the endpatch on H36.....</i>	56
Figure 5.3	<i>Non-contact profilometry scan for wear scar on sapphire counterface run against H10</i>	57
Figure 5.4	<i>Raman spectrum from coating H36 and from a transfer film on sapphire from the test run on coating H36.....</i>	58

<i>Figure 5.5</i>	<i>Friction (solid lines) and contact diameter (open circles) versus sliding cycle coatings (a) H0, (b) H8.5 and (c) H36</i>	59
<i>Figure 5.6</i>	<i>A plot of friction versus cycle number for Films H0, H8.5, H10, H14, and H36.....</i>	61
<i>Figure 5.7</i>	<i>RMS roughness versus cycles to run-in for samples H8.5, H10, H14, and H36.....</i>	63
<i>Figure 5.8</i>	<i>Cycles to run-in plotted versus intensity of the 26° XRD reflection peak intensity</i>	64
<i>Figure 5.9</i>	<i>Cycles to run-in plotted versus Pin-on-Disk friction coefficient</i>	65
<i>Figure 6.1</i>	<i>Counterface wear versus diamond coating roughness. Open circles are from Ref. 26 with roughness (Ra) calculated from line profiles from contact profilometry. Open triangles are from this work with roughness (RMS) calculated from AFM scans. The square data points are for the two tests on H0 where the counterface wore continuously throughout the test.....</i>	66
<i>Figure 6.2</i>	<i>Average number of run-in cycles versus NCD coating roughness</i>	68
<i>Figure 6.3</i>	<i>Average number of run-in cycles versus diamond orientation</i>	69
<i>Figure 6.4</i>	<i>Plots of the graphite peak (002) amplitude normalized to the sum of the diamond peak amplitudes [(111) and (220)] versus measurements from NEXAFS, including (a) the sp² content and (b) the position of the C1s→π* peak.....</i>	70
<i>Figure 6.5</i>	<i>Plots of coating properties from NEXAFS and XRD versus run-in cycles, including (a) percent sp² content, (b) normalized graphite peak amplitude and C1s→π* peak position.....</i>	72

1. Introduction

Carbon forms into many different allotropes that can be useful in deposition of thin films. These different forms or phases vary in properties and performance. These variations are largely due to bonding structure and chemical properties. Carbon films are structured similar to graphite, diamond, or they are an amorphous mix of all different types of carbon bonding possibilities. Amorphous carbon films also come also in many forms: diamond like carbon (DLC), tetrahedral amorphous carbon (t-a:C), amorphous carbon, and many others. These terms are sometimes ambiguous, but in this work these types of films are distinguished from diamond in that their bonding is not necessarily dominated by sp^3 carbon. Also within the NCD definition, it is accepted that there is small (<10% hydrogen content in the films).

Nanocrystalline diamond also covers a wide range of coating types, within the sp^3 dominated regime. These types of films are not one solid sp^3 bonded coating, but consist of crystalline “diamond grains” in an amorphous grain boundary region. Some NCD films can be further classified as ultra-nanocrystalline diamond (UNCD). To be classified as nanocrystalline, a film must have grain sizes that are on the order of 100 nm or less. Grain boundaries separate the sp^3 regions of the film and are usually composed of sp^2 bonded material. For classification as UNCD, coatings must have grain sizes smaller than 50 nm; coatings discussed here have grain sizes of 5 – 10 nm. UNCD films also have very small grain boundaries. One goal in the development NCD films to UNCD films is the reduction or elimination of grain boundaries. These types of films may have different characteristics and performance properties. Transmission Electron Microscopy studies of the coatings discussed in this work show little to no grain boundaries [1].

Nanocrystalline diamond (NCD) films have been shown to have excellent properties for a wide variety of applications including biosensors, tool coatings, and microelectromechanical systems. These films display high hardness and low roughness which make them desirable for optical, mechanical and tribological coatings. All of these applications require well characterized films to ensure their quality as related to the desired application.

Nanocrystalline diamond films can be produced using a variety of growth techniques under many growth conditions. Plasma enhanced chemical vapor deposition (PECVD) is the technique used in this study. One method to deposit NCD films is to add or substitute noble gases in the growth environment [3]. Diamond film chemical vapor deposition (CVD) processes use mixtures of hydrocarbons, usually methane, and hydrogen. It has been suggested that reactions with atomic hydrogen play the key role in diamond deposition by CVD techniques [4].

Hydrogen will play a role in both etching and growth processes. When using methane (CH_4) in a plasma enhanced CVD various dissociation processes and abstracted reactions can take place, which may form CH_2 or CH_3 in their radical form as well as ionized forms upon electron impact in second order reactions. Typically the interaction of the radicals at the substrate surface enables growth of thin films.

Atomic hydrogen is generated in the plasma by electron-molecular hydrogen collision, which dissociates the molecular form to atomic hydrogen. Ionization of dissociated hydrogen in microwave discharges can take place allowing hydrogen ions to play a role in

the deposition process. Dissociation into atomic hydrogen may also be followed by ionization to produce hydrogen ions if the energy is sufficient to induce ionization.

Methyl radicals are generated by abstraction reactions in the plasma such as the reaction $\text{H} + \text{CH}_4 \rightarrow \text{CH}_3 + \text{H}_2$. These reactions are the primary source of carbon radicals for film deposition. However, electron impact on CH_4 can also dissociate CH_4 into CH_2 plus H_2 or CH_3 plus H depending on the reaction rate constant that characterizes each reaction. The reaction rate is a function of the electron temperature and an increase in electron temperature increases the reaction rate. Electron plasma temperatures above 1 eV are sufficient to induce such reactions [5]. The abstraction reactions are key in PECVD and provide the source of carbon radicals for film deposition. These radicals bond to carbon sites on the exposed hydrogen terminated surface to form the thin film [2]. As atomic hydrogen etches graphite during film growth, sp^2 sites are preferentially removed and growth of crystalline diamond is enabled [4].

When using carbon based molecular gases such as CH_4 the ratio of the hydrogen to the carbon, H:C, plays an important roll in the process. As H:C increases, etching becomes dominant, and a decrease in this ratio leads to a reduced deposition rate, and a reduction in sp^2 bonded sites [5]. Methane appears to be an efficient gas for PECVD.

Inclusion of argon in the discharge changes the electron number density of the plasma. Due to the fact that the plasma is quasi-neutral, $n_e = \sum_j Z_j n_j$ for all j species in the plasma, the ion number density changes and alters the plasma reactions to include more ionization and dissociation reactions than hydrogen alone [6,7]. So, adding argon to a hydrogen plasma

allows for heavy ions, which are slower, to exist and participate in the surface processes. Slower species may show enhanced adhesion to the surface. When noble gasses, such as argon, are added the emission lines of carbon dimer species change. These changes in plasma reactions may directly alter the structure and morphology of diamond coatings [6, 7]. This thesis examines coatings that were deposited with varied Ar/H₂/CH₄ ratios.

As the gas mixture is composed of H₂/Ar/CH₄, several collisional processes are expected and numerous spectral lines should be observed. Dissociation of molecular hydrogen into atomic hydrogen by electron impact and ionization of molecular hydrogen and atomic hydrogen is expected in microwave discharges [5, 8]. Electron impact dissociates CH₄ into CH₃ and a hydrogen atom [5, 9]. It may also dissociate into CH₂ and release a hydrogen molecule. These reactions are second order reactions and each depends on the corresponding reaction rate constant.

Abstraction reactions result from the interaction of atoms and molecules. These reactions may take place faster because they do not need ionization energy while electron impact reactions require ionization of at least one of the working gases in the growth environment to produce electrons. If the plasma energy is sufficient, as is the case in most microwave discharges, full dissociation of CH₄ into carbon atoms and atomic hydrogen is also expected. Electron collision with carbon atoms may ionize carbon, which could be observed from optical emission spectroscopy of the plasma. It is expected that the electron plasma kinetic temperature T_e should be in the range of 3-5 eV and the number density in the range of 10^{17} - 10^{18} m⁻³ for a typical μ CVD discharge operating in the range of 800-900 W [5, 10].

Microwave discharges can operate over a wide range of pressures up to 1 atm. At low pressures, few mTorr, the electron temperature can be as high as 15 eV; as the pressure increases the temperature levels off to the range of 3-5 eV around 10 mTorr and higher; the films discussed in this thesis were deposited at 65 Torr and fit into this range. The corresponding number density will be in range of 10^{17} m^{-3} in the lower pressure range (< 1 Torr) and approaches 10^{18} m^{-3} in the higher pressure ranges (> 10 Torr). For this work the operating pressure is 65 Torr with a power of 900 W. The electron plasma density is on the order of $10^{18} / \text{m}^3$ and the electron plasma temperature is on the order of 5 eV. These results correlate to the above pressure range (> 10 Torr) of electron plasma temperature and number density [5, 9-11].

The ultimate goal to achieve in NCD deposition using $\text{H}_2/\text{Ar}/\text{CH}_4$ gas mixtures is the deposition of films with domains < 10 nm, negligible grain boundary thicknesses, and a high sp^3/sp^2 ratio.

Moving to the UNCD regime from traditional CVD-grown microcrystalline diamond coatings (MCD) and NCD coatings has been made possible through the development of new growth techniques. Figure 1.1 shows the difference between MCD, NCD, and UNCD film nucleation and growth patterns. MCD (1.1a) deposition favors growth of existing domains rather than re-nucleation of new growth sites, which is favored by NCD (1.1b). The continued growth in MCD results in structures that are tens or hundreds of microns in size. These structures are rough faceted and lead to a rough film surface.

Conversely in NCD growth, new sites are nucleated frequently. This results in much smaller bulk structures that are on the order of 100 nm. This also leads to smoother surfaces

since they do not increase in size as the film grows. Films that have been termed UNCD, as shown in 1.1(c), also re-nucleate but as discussed above more sp^2 sites are etched and grain boundaries widths are reduced to the minimum obtainable. Pre-nucleation techniques and various gas mixtures including hydrogen, argon, and methane in PECVD systems, have been shown to result in films with grain sizes in the range of 2-10 nm and RMS surface roughness below 50 nm [12-19].

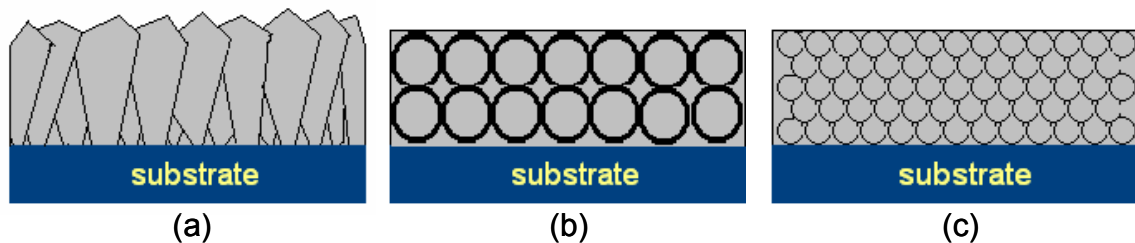


Figure 1.1 – Schematic showing the differences in nucleation and growth of (a) microcrystalline diamond with large growth domains, (b) nanocrystalline diamond with smaller domains and relatively thick grain boundaries, and (c) ultra-nanocrystalline diamond films with minimum achievable grain size and grain boundary thickness.

Bulk and surface properties of coatings influence coating friction performance.

Recent tribological studies on NCD coatings showed a period of initially high friction, called run-in, before low friction coefficients were achieved [20, 21]. For NCD to be used as a coating material, low friction with minimal run-in is desired.

Run-in behavior is often correlated to the initial interactions between the asperities of two surfaces. This process results in locally high contact stresses that lead to plastic deformation, wear and the creation of transfer films [22, 23]. For a solid wear resistant coating, the reduction in friction following this stage is typically associated with the formation of a stable transfer film [23, 24]. Diamond also follows this trend of high friction run-in with wear followed by low friction. It has been speculated that the low friction

mechanism for diamond arises from the formation of a thin, less-dense carbon transfer layer, possibly graphitic in nature [25-27].

With the aim of understanding and controlling the bonding and surface morphology of these coatings, the NCD films discussed here have been characterized by surface and bulk techniques. Specifically Raman spectroscopy, scanning electron microscopy, transmission electron microscopy, atomic force microscopy, x-ray diffraction, and near edge x-ray absorption fine structure spectroscopy (NEXAFS) were all employed to characterize the films.

Determination of bonding coordination is made primarily by NEXAFS. Raman spectroscopy and x-ray diffraction have also provided structural information. Raman is sensitive to carbon bonding configurations, but the resonance effects due to sp^2 bonded carbon require another technique, such as NEXAFS and XRD, to provide a quantitative analysis of proportions of different bonding environments, i.e. sp^2/sp^3 ratio.

Along with bonding structure, observing surface morphology is also important in understanding the growth process for these coatings, especially for tribological applications. Using AFM and SEM, trends in morphology are observed and correlated with growth conditions and structural information. Understanding the variation in structure with growth conditions will allow for better control of film characteristics, and subsequent optimization of tribological performance.

Tribological performance depends on both the surface and bulk properties, such as hardness and fracture resistance, of the material. NCD has high hardness and tensile strength, approaching that of single crystal diamond. The reduction of grain size and elimination of

grain boundaries moves NCD and UNCD films closer to single crystal diamond in performance [12]. Therefore, the goal of deposition in the UNCD regime is to eliminate large surface and bulk structures that could be susceptible to shearing and stress to improve the performance and durability of coatings.

Deposited material properties can be controlled via CVD processes, “which consists of a thermally activated set of gas-phase and surface reactions that produce a solid product at the surface [5].” Better control of the growth process is achieved using PECVD in which the gas phase and the surface reactions are controlled by the plasma parameters. Electron impact dissociation of the feedstock gas plays an important role, such that deposition can be achieved at temperatures lower than CVD [5].

Diamond on diamond and sapphire on diamond tribological studies on MCD coatings have recognized that surface roughness plays a critical role for run-in and the eventual steady-state friction [4, 25, 28-32]. For diamond on diamond sliding, low friction and short run-in is only achievable on highly-polished diamond coatings. Other counterface materials can result in departures from this behavior. For example, Hayward et al studies [29, 30] for sapphire versus diamond sliding demonstrated that the roughness of the diamond coating affected the wear of the sapphire counterface as well as the friction properties. Low friction was eventually observed, but at the expense of extensive counterface wear. Bull, et al. [32] conducted a similar study of sapphire sliding versus MCD coatings and found a regime of continuous high friction that was independent of coating roughness. The difference between these two studies may be a reflection on the performance of the various diamond coatings, possibly with respect to their ability to form a transfer film [24].

In this thesis the tribology of nanocrystalline diamond coatings grown in a H₂/Ar/CH₄ microwave plasma discharge with gas phase hydrogen content ranging from 0 to 36% is examined. An *in situ* tribometer with a sapphire counterface was used, allowing for examination of the sliding contact during tribology experiments [23, 24].

The materials discussed here have been well characterized by surface and bulk techniques including Raman Spectroscopy, Atomic Force Microscopy, Transmission Electron Microscopy, Scanning Electron Microscopy, X-ray Diffraction, and Near Edge X-ray Absorption Fine Structure Spectroscopy. Performance of the NCD coatings was characterized by both the extent of high friction run-in and measurements of the *in situ* contact diameter, a quantity related to counterface wear. Coating performance is linked to roughness, chemistry, and the formation of transfer films on the sapphire counterfaces.

This thesis is organized as follows: Chapter 2 discusses the Deposition of NCD coatings. Chapter 3 discusses the characterization and analysis of the NCD coatings described in Chapter 2. This is followed by a discussion of the plasma environment in Chapter 4. Chapter 5 is dedicated to the tribology of NCD coatings. Finally, conclusions and future directions of this work are discussed in Chapters 6 and 7.

2. Deposition of NCD Coatings

2.1 Chemical Vapor Deposition

The nanocrystalline diamond coatings discussed in this work were prepared using a microwave plasma enhanced chemical vapor deposition system (1.5 kW ASTeX 2.45 GHz). Chemical vapor deposition is a process in which deposition of species on a substrate takes place at the gas phase interface. The process is thermally assisted, controlled, or limited and in many processes the temperature required may be as high as 800-900 °C. Plasma enhanced chemical vapor deposition (PECVD) allows for controllability of the process via adjustment of the plasma parameters, specifically plasma temperature and density. Changing deposition conditions such as pressure and microwave power directly affects the plasma parameters.

Changing the pressure,

$$P = \sum_j n_j K T_j \quad (1)$$

where j is all plasma species, changes the number density and temperature. Increasing the input power increases the effective power dissipated into the plasma, which in turn increases the fractional ionization as well as the kinetic temperature of the plasma [5, 33].

Deposition of thin, uniform diamond films on substrates using PECVD highly depends on understanding and control of the species in the plasma, the surface, and the nucleation processes [16, 17]. In this work the focus is on the contribution of various reaction rates from the hydrogen/argon/methane plasma and the effects of increased argon content in the growth environment. A description of the theory of microwave heating follows along with a description of the device and deposition conditions.

2.1.1 Microwave Discharges

Wave-heated discharges are characterized by the form with which an electromagnetic wave interacts with plasma. Due to the fast response of electrons to changes in the electric field, most wave-heated discharges are characterized by electron heating and thus higher electron plasma temperatures can be achieved. Electron number density ranges $\sim 10^{16} - 10^{20}$ /m³, depending on microwave input power and the discharge chamber base pressure. It has been shown that typical values of electron number densities are in the range of 3×10^{18} /m³ [5, 9, 10].

Wave-heated discharges may be arranged in various forms, with or without magnetic field, and at various length-to-radius ℓ / R ratios, known as the discharge aspect ratio, in which ℓ represents the cavity length and R is the cavity's radius [5]. Figures 2.1(a) and 2.1(c) show simplified drawings of low and high aspect ratio wave-heated discharges [5]. Wave-heated discharges are commonly known as microwave discharges in which the microwave source is coupled to the plasma chamber via a waveguide, and hence it is a resonant or multimode cavity discharge [8].

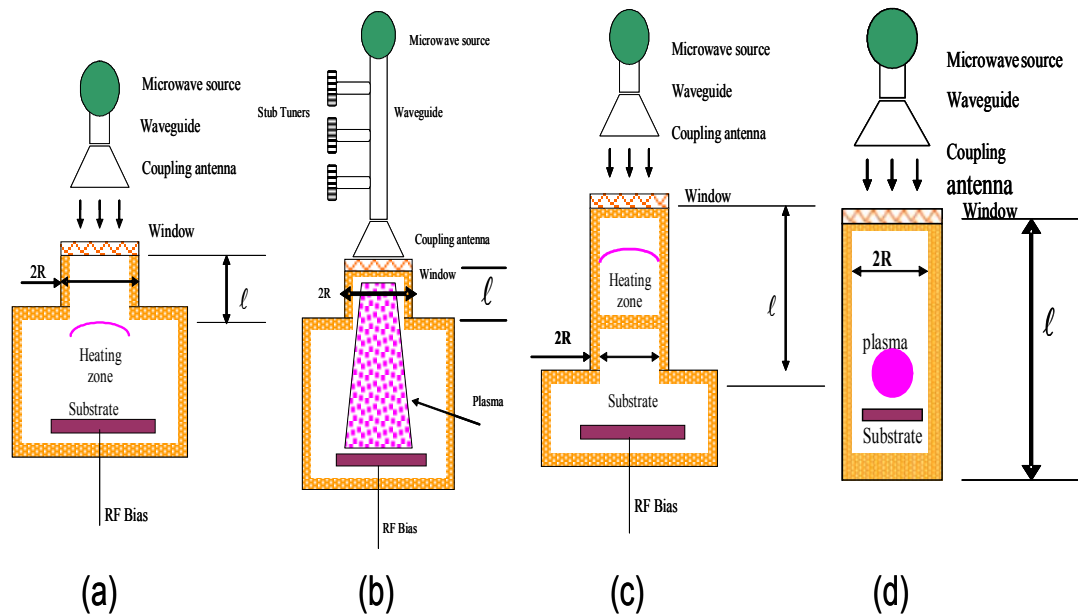


Figure 2.1 (a) Low aspect ratio microwave discharge; the heating zone is close to the cavity exit at the interface with the discharge chamber. (b) Coupling microwave source to waveguide and plasma via stub tuners for maximum forward and minimum reflected power, plasma takes a conical shape as it emerges from the cavity into the reaction chamber. (c) High aspect ratio microwave discharge, the heating zone is inside the cavity and may be close to the launching window. (d) High aspect ratio single cavity discharge, similar to that used in this thesis, plasma forms a spherical shape on top of the substrate.

The microwave source must be coupled to the cavity via a waveguide adequate for the launching mode (TE_{10} rectangular, TE_{11} circular, or TM_{01} circular) [5]. Coupling to the plasma chamber is typically achieved through a waveguide with a coupling stub tuner waveguide for maximizing the forward power and minimizing the backward (reflected) power. Figure 2.1(d), which represents the system used in this thesis, shows a setup with a 3-stub tuner waveguide in a low-aspect ratio discharge, the plasma takes a conical shape as the flow emerges from the cavity towards the reaction chamber. If the discharge is arranged with magnets to operate in the electron cyclotron resonance (ECR) mode, the electron heating

mechanism is determined by the electron cyclotron resonance frequency, $\omega_{ce} = \frac{eB}{m_e}$ where e is the electron charge in Coulombs, m_e is the electron mass in kg, and B is the magnitude of the magnetic field in Tesla. For most microwave discharges used in plasma-enhanced chemical vapor deposition (PECVD) the operating frequency is 2.45 GHz and thus the wavelength is 12.24 cm, which is the free space wavelength. The cavity dimensions with respect to the free space wavelength determine the discharge mode, a resonant cavity discharge is when the cavity dimensions are comparable to the free space wave length and a multimode cavity is when the dimensions are much larger than the free space wavelength [8]. In this thesis work, the cavity diameter is about 2λ .

In microwave discharges the electric field oscillates with the frequency of the power supply and a breakdown electric field value for the working gas must be reached in order to form and self-sustain the plasma. A definition of the effective breakdown electric field E_{eff} for collisional un-magnetized plasma, Eq. (2), which ignites the plasma, was given by J. Reece Roth [8] as related to the amplitude of the wave's electric field \tilde{E} in V/m, the microwave frequency ω and the collision frequency ν_c :

$$E_{eff}^2 = \tilde{E}^2 \frac{\nu_c^2}{\omega^2 + \nu_c^2} \quad (2)$$

The power P in Watts absorbed by a single electron is given by [8]:

$$P = \frac{e^2 E_o^2}{2m_e \nu_c} \left(\frac{\nu_c^2}{\omega^2 + \nu_c^2} \right) \quad (3)$$

Where e is the unit electric charge, E_o is the amplitude of the electric field, m_e is the electron mass in kg, and ω and ν_c are the oscillating and collision frequencies, respectively. Hence, the total power absorbed by plasma electrons would be $P_{tot} = P n_e$, where n_e is the electron number density in the plasma.

$$P_{tot} = \frac{e^2 E_o^2}{2m_e \nu_c} \left(\frac{\nu_c^2}{\omega^2 + \nu_c^2} \right) n_e \quad (4)$$

To transfer the absorbed power to the energy absorbed from the electric field, $\mathcal{E}_{absorbed}$ (in Joules), one has to include the collision time by dividing the power by the collision frequency [8] and hence:

$$\mathcal{E}_{absorbed} = \frac{P_{tot}}{\nu_c} = \frac{e^2 E_o^2}{2m_e \nu_c^2} \left(\frac{\nu_c^2}{\omega^2 + \nu_c^2} \right) n_e \quad (5)$$

In collisional plasmas, where the electron mean free path is short, the collision frequency ν_c is much greater than the microwave frequency ω Equation (5) can be simplified to:

$$\mathcal{E}_{absorbed} \cong \frac{e^2 E_o^2}{2m_e \nu_c^2} n_e \quad (6)$$

Equation (6) represents the microwave energy needed to ignite and sustain the plasma and is an appropriate approximation for the 65 Torr plasmas discussed in this thesis. For plasmas that are less collisional ($\omega \gg \nu_c$), Equation (5) may be approximated to:

$$\mathcal{E}_{absorbed} \cong \frac{e^2 E_o^2}{2m_e \omega^2} n_e \quad (7)$$

The above equation is applicable to low pressure plasmas (mTorr range) where the electron mean free path is longer than in high pressure plasmas (1-760 Torr).

Absorbed power from Eq. (4) may be used to obtain an estimate of the electron number density assuming the total power absorbed is consumed into ionization

$$n_e = P_{tot} \frac{2m_e \nu_c}{e^2 E_o^2} \left(\frac{\omega^2 + \nu_c^2}{\nu_c^2} \right) \quad (8)$$

When most of the input power goes to ionization, the input power P is related to the ionization frequency ν_i and ionization energy \mathcal{E}_{iz} , as $P = \nu_i e \mathcal{E}_{iz}$ [8]. A substitution for the ionization frequency utilizing Eq. (3) gives

$$\nu_i = \frac{P}{e \mathcal{E}_{iz}} = \frac{E_o^2}{\mathcal{E}_{iz}} \frac{e}{2m_e \nu_c} \left(\frac{\nu_c^2}{\omega^2 + \nu_c^2} \right) \quad (9)$$

Using the ionization frequency from the kinetic theory with the electron velocity taken as the thermal velocity over a Maxwellian distribution, then [8]:

$$\nu_i = \frac{8eT_e}{3\pi \nu_c m_e \Lambda^2} \quad (10)$$

Where T_e is the electron plasma temperature (eV) and Λ is the diffusion length given by

$$\Lambda = \left(\frac{1}{\left(\frac{\pi}{\ell} \right)^2 + \left(\frac{2.405}{a} \right)^2} \right)^{\frac{1}{2}} \text{ for cylindrical plasma. Here } \ell \text{ is the length of the discharge, } a \text{ is}$$

the radius of the plasma, and the 2.405 is root of the zero order Bessel function for the solution of diffusion equation in cylindrical geometry [8].

From Eq. (9) and (10), Roth [8] provided a solution for the ionization energy \mathcal{E}_{iz} as

$$\mathcal{E}_{iz} = \frac{3\pi}{16} \Lambda^2 \frac{E_o^2}{T_e} \left(\frac{v_c^2}{\omega^2 + v_c^2} \right). \text{ A solution for the electron plasma temperature is an important}$$

parameter in determining the nature of the plasma. It affects the various reaction rate coefficients for electron impact on heavy species. Solving for the electron plasma

temperature gives $T_e = \frac{E_o^2}{\mathcal{E}_{iz}} \frac{3\pi}{16} \left(\frac{v_c^2}{\omega^2 + v_c^2} \right) \Lambda^2$ and substituting for Λ one can obtain an

expression for the electron temperature:

$$T_e = \frac{E_o^2}{\mathcal{E}_{iz}} \frac{3\pi}{16} \left(\frac{v_c^2}{\omega^2 + v_c^2} \right) \left(\frac{1}{\left(\frac{\pi}{\ell} \right)^2 + \left(\frac{2.405}{a} \right)^2} \right) \quad (11)$$

Again, for $v_c \gg \omega$) Eq. (11) reduces to:

$$T_e \cong \frac{E_o^2}{\mathcal{E}_{iz}} \frac{3\pi}{16} \left(\frac{1}{\left(\frac{\pi}{\ell} \right)^2 + \left(\frac{2.405}{a} \right)^2} \right) \quad (12)$$

And for $\omega \gg v_c$ Eq. (11) reduces to:

$$T_e = \frac{E_o^2}{\mathcal{E}_{iz}} \frac{3\pi}{16} \left(\frac{v_c}{\omega} \right)^2 \left(\frac{1}{\left(\frac{\pi}{\ell} \right)^2 + \left(\frac{2.405}{a} \right)^2} \right) \quad (13)$$

It is evident that one can obtain a measure of the electron plasma temperature based on the assumption that all microwave power is absorbed in the plasma and consumed into ionization. Both Eq. (9) and (11) are useful in determining plasma parameters in a microwave discharge, however, the temperature and density are average values over the entire discharge.

For a determination of the temperature and density distribution, one has to use other techniques such as optical emission spectroscopy or electric probes to scan the entire discharge.

To apply the model to the microwave discharge in this thesis, one can substitute

known parameters in Eq. 11 $T_e = \frac{E_o^2}{E_{iz}} \frac{3\pi}{16} \left(\frac{\nu_c^2}{\omega^2 + \nu_c^2} \right) \left(\frac{1}{\left(\frac{\pi}{\ell} \right)^2 + \left(\frac{2.405}{a} \right)^2} \right)$ and compare the

results to experimental ones. The collision frequency ν_c is given by $[2.37 - 5.3 \times 10^9]$ multiplied by the pressure (in Torr) [34, 35]. For the system used in this thesis work, $\nu_c \sim 1.659 - 3.71 \times 10^{11}$ Hz and pressure is 65 Torr. Taking an average of $\nu_c = 2.5 \times 10^{11}$, and $\omega = 2\pi \times 2.45 \times 10^9$ Hz, hence $\left(\frac{\nu_c^2}{\omega^2 + \nu_c^2} \right) \cong 0.996$. With $\ell = 40$ cm and a is about 5 cm

then $T_e \cong \frac{E_o^2}{\mathcal{E}_{iz}} \times 2.4486 \times 10^{-4}$. $E_o \sim 600$ V/m and \mathcal{E}_{iz} is 13.6 eV for hydrogen, 15.8 for argon,

and 12.6 for methane, hence solving for the highest of 15.8 for argon yield $T_e = 5.6$ eV, about 6.48 eV for hydrogen and 7 eV for CH₄. Optical emission spectra have shown T_e for a pure hydrogen discharge to be 4.28 eV and for the mixed Ar/H₂/CH₄ and about 4.7 eV for 2% methane in a 98% hydrogen plasma. The model with its simplified assumptions yields favorable results as compared to experimental measurements. These values are consistent with a recent study by May et. al.. They reported electron kinetic temperature of 2.4 – 3 eV for a 1% CH₄/ 2% H₂/ 97% Ar mixture at 100 Torr [10]. Their values are somewhat lower than the values measured in this work via optical emission spectroscopy, discussed in

Chapter 4, because their system was operated at 800 W, which is 100 W less than the power used in this thesis.

The above technique in modeling the plasma in a microwave discharge was investigated by Yamada et al for their work on microwave plasma discharge for chemical vapor deposition of diamond [9]. In their model they equated the absorbed power P_{abs} , which is equal to the total power previously given in Eq. 3, to the sum of powers for all reactions

between electrons and heavy species $\sum_s E_s n_s k_s e^{-\frac{E_s}{T_e}}$, where k_s is the rate coefficient for all ionization, recombination, dissociation and excitation reactions between electrons and heavy species, n_s is the number density of heavy species ($n_s \approx n_e$ for quasi-neutral plasma) and E_s is the threshold energy for these reactions, and T_e is the electron plasma temperature.

They proposed a technique to solve the equation $P_{absorbed(total)} = \frac{e^2 n_e}{2m_e} \frac{v |\hat{E}|^2}{\omega^2 + \nu_c^2} = \sum_s E_s n_s k_s e^{-\frac{E_s}{T_e}}$

for T_e by equating the equation to an equivalent exponential form $P_L e^{-\frac{E_L}{T_e^{\alpha_L}}}$ in which P_L is an equivalent power, E_L equivalent reaction energy and $T_e^{\alpha_L}$ is an equivalent electron kinetic temperature raised to a fitting power factor α_L ($=0.36757$). By adopting this technique they obtained an expression for the electron plasma temperature given by [9]:

$$T_e = \left(\frac{E_L}{\ln \left\{ P_L / P_{absolute(total)} \right\}} \right)^{1/\alpha_L} .$$

Their model can be used to obtain spatial distribution of temperature and density because the model includes the electric field distribution. Their results, numerical and

experimental, are in good agreement, showing an electron number density of about $1.8 \times 10^{18} / \text{m}^3$ and an average electron plasma temperature of 1.5 eV for a methane discharge at 160 Torr and 1.6 kW microwave power. Yamada et al. also reported that an increased accuracy may be obtained if other parameters, such as pressure and boundary conditions, would be either known or measured. Their model and above models in Eq. (9) and (12) could be used to compare to each other and to verify plasma parameters in PECVD discharge and benchmark experimental results [9].

2.1.2 NCD Deposition Technique

Nanocrystalline diamond coatings were prepared using a microwave plasma enhanced chemical vapor deposition system (1.5 kW ASTeX 2.45 GHz). The gases used for deposition were argon, hydrogen, and methane. Coatings were deposited on single side polished silicon (100) wafers after a seeding process. Samples were grown at 900°C and with a microwave power of 900 W in a chamber at 65 torr. The total gas flow was 70 sccm with CH_4 flow set to 7 sccm for all coatings. Flow rates of argon and hydrogen were varied from sample to sample, with the hydrogen ranging from 0 to 36% of the total gas flow. The coatings discussed in this study are denoted to by the percent of hydrogen in their growth plasma:

$$H\# = \frac{[H_2]}{[H_2] + [Ar] + [CH_4]} \quad (14)$$

The H# refers to the percent of hydrogen gas in the total flow of gasses during coating growth. Bracketed quantities are the flow rates of the feed gasses during the growth process.

The hydrogen flow rates were: 0, 6, 7, 10, and 25 sccm, and the argon flow rates were 63, 57,

56, 53, and 38 sccm, where each of the quantities represent the flow rates of the specific gases. Based on these flow rates and Eq. 14 five different coatings were prepared: H0, H8.5, H10, H14 and H36. Figure 2.2 is a diagram of the system used.

The system is composed of a plasma chamber coupled to the microwave generator via a microwave window. The substrate sits on a sample stage, which is part of the induction heater assembly. Samples are loaded by removing the heater from the bottom of the device and sit on a molybdenum or quartz stage. The induction heater is controlled via a separate power supply, and the substrate temperature is monitored both by a thermocouple and an external pyrometer. A helium-neon laser is used to monitor film growth via interferometry. Viewing windows allow for visual inspection of the plasma and substrate. Gas mixing ratios are controlled by MKS gas flow meters and flow controllers.

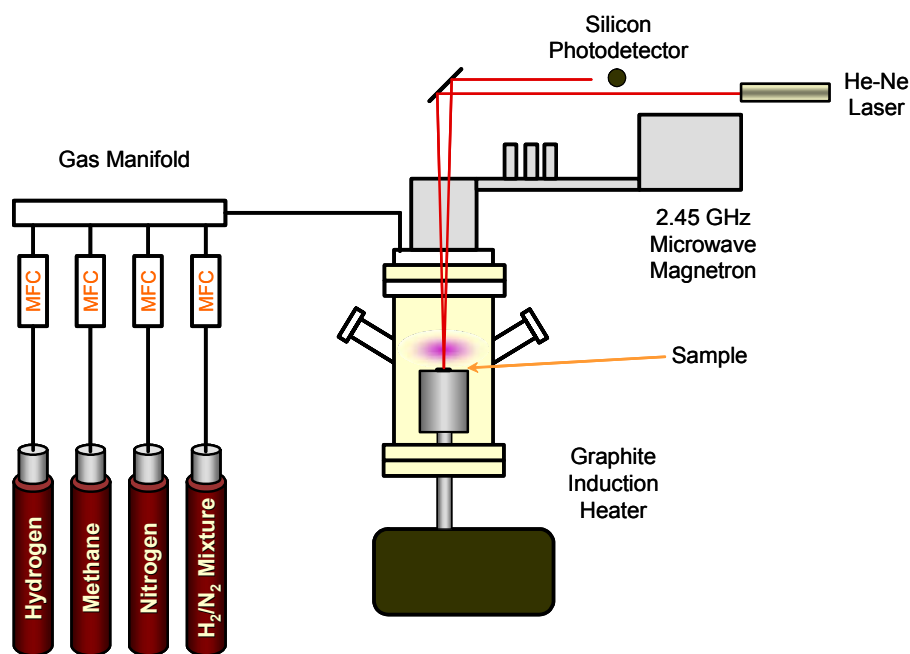


Figure 2.2 – Schematic of the microwave PECVD system used for the films in this thesis. In addition to deposition on silicone wafers, ¼ inch diameter sapphire hemispheres were employed on for self mated friction experiments.

3. Materials Characterization and Analysis of NCD Coatings

3.1 Surface Morphology: Atomic Force Microscopy and Scanning Electron Microscopy

Figure 3.1 shows scanning electron microscopy (SEM) images of three films (H0, H8.5 and H36). All of the films display roughness on about 1 μm scale and a needle-like morphology at the finest scale. Variations in surface morphology are seen with changes in the growth environment. In particular, the scale of the morphology (i.e. the size of the growth domains) increases with increasing H% in the plasma increases. This was particularly apparent for sample H36 (see Figure 3.1). The variation in morphology may impact tribological performance.

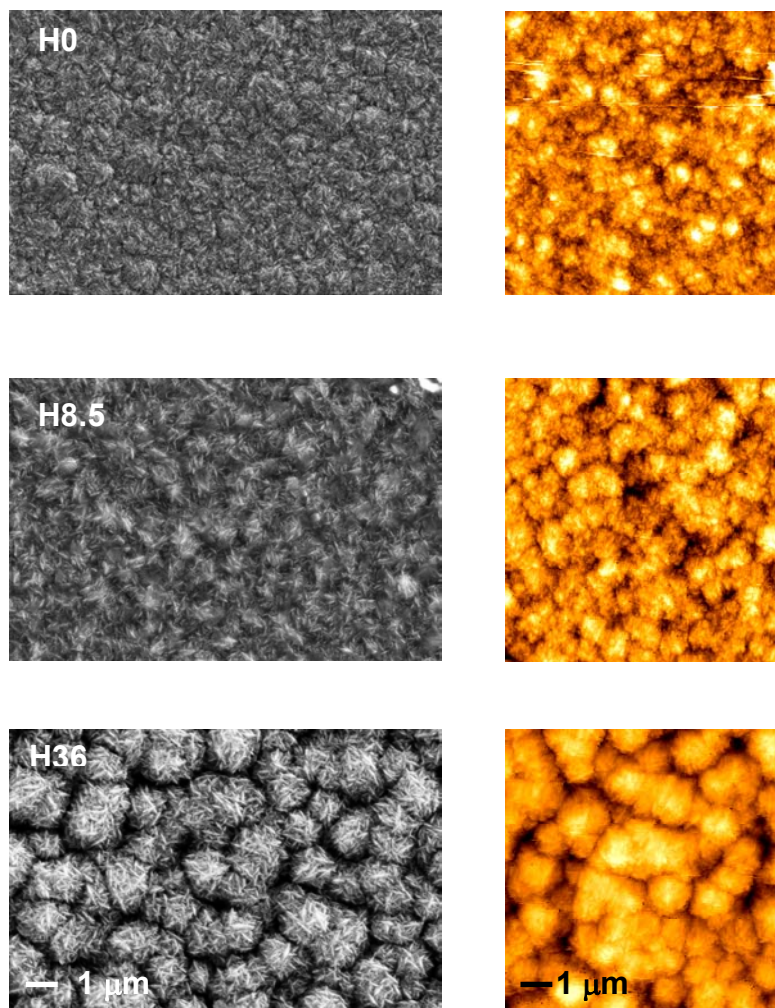


Figure 3.1 – SEM and AFM images films grown in different plasma environments. H# refers to the percent of H₂ in the total gas flow.

The morphology of as-prepared coatings and wear tracks were examined in a LEO Supra50 scanning electron microscope. The accelerating voltage was either 5 or 10 keV. Qualitative chemical identification was carried out with an Oxford Instruments energy dispersive spectrometer (EDS). These measurements are discussed in detail in Chapter 5 and illustrated in Figure 5.2.

Additional examination of the sample morphology was carried out with a Veeco Nanoman Dimension series atomic force microscope (AFM). The instrument has closed loop scanning capabilities for quantitative analysis of surface topography and roughness characterization. Scans were conducted at varying sizes ranging from 1 to 40 μm . The roughness values reported here were calculated from the 10 μm scan size images.

The small needle-like features and variation in morphology are also observed in the atomic force microscopy (AFM). Roughness was determined from the scans and found to be between 20-60nm for a 10 μm x 10 μm scan size. RMS roughness results are listed in Table 3.1.

Table 3.1 – Characteristics of the nanocrystalline diamond coatings determined from AFM, x-ray diffraction, and NEXAFS. The intensity of the graphite peak varied from sample to sample and is normalized to the sum of diamond (220) and (111) peak intensities.

	RMS Roughness (nm)	NCD Grain Size (nm) Scherrer	Strain (x 10⁻³)	Lattice Constant (Å)	Strain	Grain Boundary Peak Amplitude	sp² content
H0	28	10	-2.5	3.5599	-2	-	11
H8.5	30 \pm 2	7.2	-6	3.5612	-1.5	9	20
H10	26	8.8	-5	3.5599	-2	6	16
H14	40	7.5	-0.1	3.5582	-2	8	14
H36	56	10.4	-0.4	3.5563	-3	13	15

Roughness measured by AFM is presented in Table 2.1; roughness increased with hydrogen content of the growth plasma. We note that roughness of the coating is expected to correlate with growth domain size rather than grain size. This study did not specifically examine how the RMS roughness correlated with deposition conditions, since it appears that the nucleation is a more significant effect. The effects of nucleation are discussed in Chapter 1 and illustrated in Figure 1.1.

The SEM and AFM images also show a change in surface morphology and roughness as the argon concentration in the growth environment changes. Small, needle-like structures appear on the surface of films while larger scale morphology decreases with increasing argon concentration in the growth plasma. The RMS roughness also decreases with higher argon concentration, but this could also be related to the film nucleation seeding process.

3.2 Raman Spectroscopy

Raman spectra of the NCD films are shown in Figure 3.2. These spectra exhibit features typically associated with nanocrystalline diamond. The spectral features are broad bands at 1350 and 1520-1580 cm^{-1} with shoulders at 1100-1150 cm^{-1} and 1430-1470 cm^{-1} . The peaks at 1350 and 1580 cm^{-1} are the D and G modes characteristic of amorphous or diamond-like carbon [36]. The 1150 cm^{-1} shoulder has been associated with nanocrystalline diamond [37] as has the 1470 cm^{-1} feature [38]. These two features have been attributed to the presence of sp^2 bonded carbon in the grain boundaries and have been associated with hydrogen containing structures [37, 38].

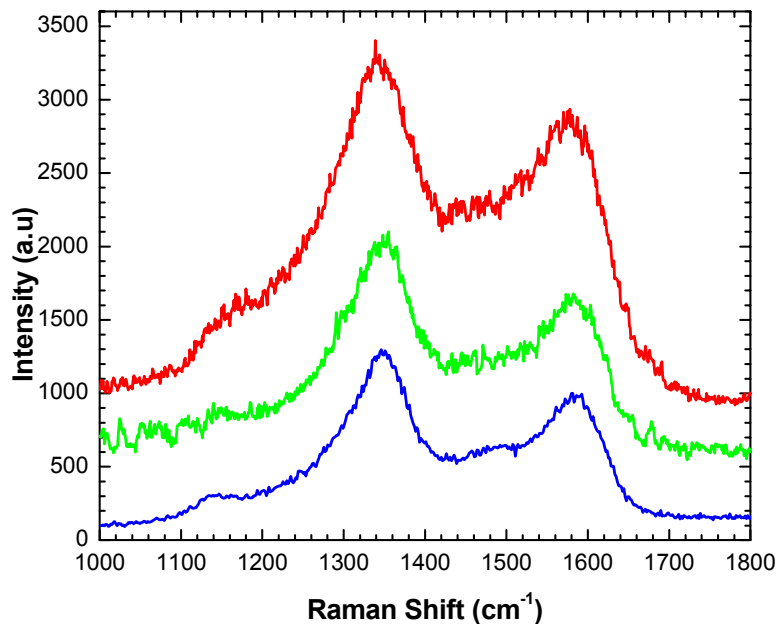


Figure 3.2 – Raman spectra for samples H0, H8.5 and H36 obtained with 514 nm excitation.

Of interest in the spectra are the position of the G peak and the shape of the D and G peak. The G peak can have a shift in position due to change in structure [35, 36]. In spectra of amorphous carbon, the position of the G band can be shifted significantly if the sp^2/sp^3 ratio of the film varies [39-47]. In this study the G peaks of the samples are not significantly shifted from each other, which could be an indication of similar sp^2/sp^3 ratios in the coatings. The size and shape of the D and G bands are also very similar. The broad, indistinct peaks indicate a low amount of order in the sp^2 bonded material

Raman spectroscopy, during *in situ* tribometry, was performed on coatings and counterfaces using a Renishaw System 1000 Raman Microprobe. Two lasers were used. Visible Raman was conducted with an Ar^+ ion laser (514 nm) focused to a spot of less than 2

μm . Near infrared was also conducted using a diode laser (785 nm) in line focus mode ($\sim 20 \mu\text{m} \times 2 \mu\text{m}$).

3.3 X-Ray Diffraction

X-ray diffraction was conducted on the coatings using a standard θ - 2θ geometry with a 3 degree offset of the goniometer axes to minimize the intensity of the Si substrate peak. The x-ray radiation was Cu, filtered with a Ni foil such that the wavelength, λ , was 0.15418 nm. Samples were examined over the range of $2\theta = 20$ to 100 degrees. Diffraction peaks were fit to a Lorentzian function using standard peak-fitting software. From these measurements, the average lattice spacing and two estimates of the grain size were calculated [48-53]. First, the method of integral breadths [48], also called the Williamson-Hall plot method [49], was applied using the relation:

$$\beta_{1/2} \cot \theta = \frac{0.9\lambda}{D \sin \theta} + 4\varepsilon \quad (15)$$

where $\beta_{1/2}$ is the full-width half-maximum (FWHM) of the peak and θ is half the detector angle for the peak position. Estimates of the grain size and the lattice strain, ε were found from a linear fit to a plot of $\beta_{1/2} \cot \theta$ versus $1/\sin \theta$. Additionally, the Scherrer formula was used to calculate a grain size, D , from the (111) diamond peak:

$$D = \frac{0.9\lambda}{\beta_{1/2} \cos \theta} \quad (16)$$

We note that the Scherrer formula may be derived from Eq. 15 with an assumption of zero lattice strain. Other researchers that have studied CVD diamond coatings have found that the stress state of their coatings is complex [50-53], possibly due to twinning [52, 53].

This leads to additional broadening of the x-ray lines that makes Eq. 15 difficult to apply. For this reason, we report the results of both methods.

X-ray diffraction spectra for NCD coatings H0, H8.5 and H36 are shown in Figure 2.5. All coatings studied exhibited the (111), (220) and (311) peaks for diamond with different intensity ratios. Thus, crystallographic orientation varied among the coatings studied. Using a qualitative analysis for diamond orientation [13], coatings H0, H10, H8.5 and H14 were all found to have a weak (110) texture. Coating H36 was found to be weakly (111) textured (see Table 3.1).

In Figure 3.3, the spectra for H8.5 and H36 also exhibited a broad, low intensity peak at roughly 26° , consistent with the (002) reflection for graphite. The peak appeared for all coatings except H0. The presence of this peak indicated a trace amount of nanocrystalline graphite in these NCD coatings. Using the Scherrer formula (Eq. 16), the grain size was estimated as between 3-5 nm. The intensity of the graphite peak varied from sample to sample and is given in Table 3.1 normalized to the sum of diamond (220) and (111) peak intensities.

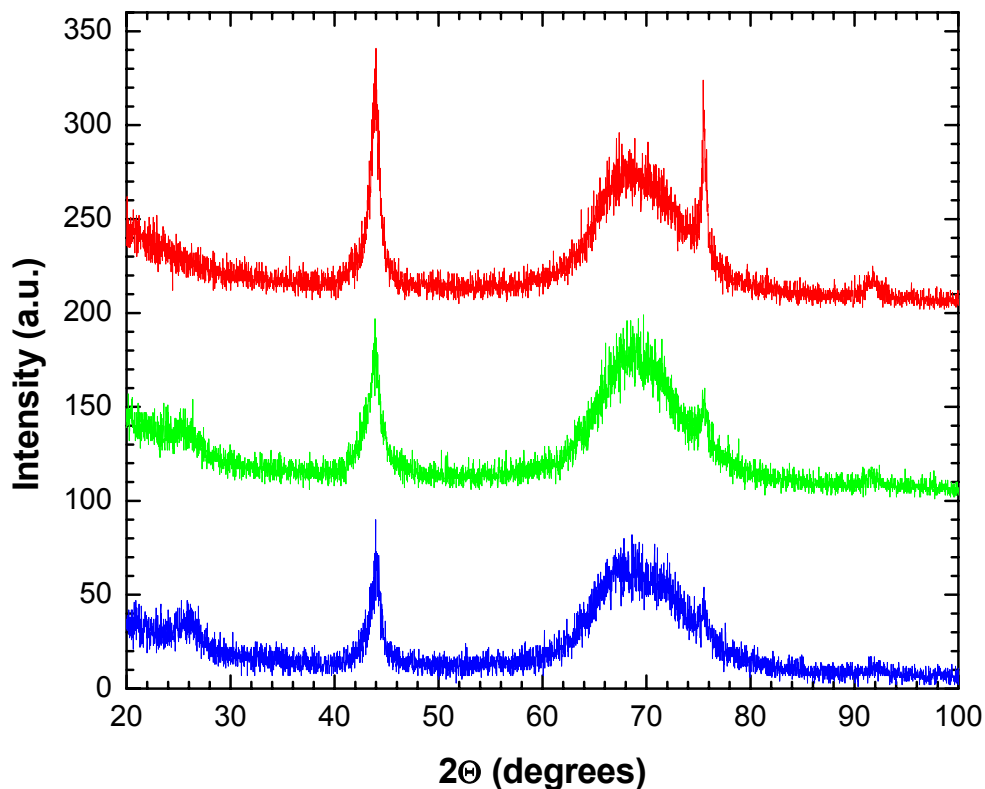


Figure 3.3 – X-ray diffraction scans showing diamond (111), (220), and (311) peaks for samples H0, H8.5, and H36.

Further results from the x-ray diffraction studies revealed a number of key features regarding the NCD coatings. Grain size estimates, average lattice constant and estimated lattice strain are all listed in Table 3.1. For all samples, the lattice constant was found to be slightly less than the value of bulk diamond ($a = 0.35668$ nm), indicating that the stress state of the coatings was compressive. The method of integral breadths was used to estimate the lattice strain. All samples exhibited negative (compressive) strain, consistent with the lattice constant results.

Grain size estimates from these two methods are generally considered to be a lower limit, especially when examining CVD diamond coatings. Both Silva, et al. [53] and Fayette, et al. [52] showed that the stress state of diamond coatings is complex and typically results in a non-linear trend on a Williamson-Hall plot. One reason for the complex stress in these coatings was determined to be twinning. This microstructural feature was shown to result in additional satellite peaks about the (111) x-ray reflection and additional broadening of the (111) line itself. Williamson-Hall plots for specimens using the (111), (220) and (311) reflections resulted in confident fits except for coatings H0 and H14. Bachmann, et al. [50] recognized the difficulty with the Williamson-Hall analysis and suggested that the Scherrer grain size is a better estimate. Based on the results in Table 3.1 and regardless of the analysis technique used, the estimated diamond grain size for the NCD coatings lies between 5 and 11 nm. XRD results are consistent with measurements from transmission electron microscopy (TEM) conducted on similar coatings [1].

From x-ray diffraction studies two trends were recognized. First, as the H% was increased the films tended to exhibit a change of the average orientation from (110) to (111). Second, as the H% was increased in the growth plasma, the intensity of the XRD peak for graphitic structures increased. This result indicated an increase in sp^2 bonded carbon that has enough long-range crystalline order to provide a diffraction signal. Because the sp^2 content measured by NEXAFS was essentially constant with changing H%, a complementary decrease in disordered sp^2 material likely occurs with the increase in crystalline graphite found by XRD. The width of the graphitic peak is consistent with a nanocrystalline grain size, and it is expected that the sp^2 bonded carbon resides predominantly in the grain

boundaries. Thus, if the grain boundary size changes with deposition conditions, changes in the amount of crystalline sp^2 graphitic material in the grain boundaries could occur.

3.4 Near Edge X-ray Absorption Fine Structure

The NEXAFS measurements were carried out by Jan Lüning at SSRL.

Near Edge X-ray Absorption Fine Structure spectroscopy was used for quantitative determination of the elemental and chemical bonding environment through the determination of a sample's sp^2 carbon bonded content. Soft X-ray absorption measurements were made at the wiggler beam line 10-1 of the Stanford Synchrotron Radiation Laboratory (SSRL). The spherical grating monochromator of this beam line covers the photon energy range from 250 to 1200 eV. Spectra were recorded for the NCD samples over the range of 270 – 470 eV. Scans were recorded by monitoring the total electron yield, TEY [54]. The number of incoming photons was monitored by the TEY signal of an 80% transmissive Au net. Both drain currents were recorded with a Keithley 427 Current Amplifier. The ratio of sample signal and incoming photon flux is then the TEY spectrum of interest measuring the sample's absorption coefficient.

NEXAFS spectra for the NCD coatings are shown in Figure 3.4. The HOPG spectrum used in data analysis is shown as well. The NCD coatings showed a feature at 302 eV that is related to the diamond second band gap [55, 56]. The spectra also display a feature at about 285 eV that arises from the excitation of C1s electrons to the unoccupied π^* states attributed to sp^2 (C=C) and, if there are any, C \equiv C sites. We note that as the deposition conditions changed (greater H content in the source gas), the position of the 1s to π^* transition changed from 285.0 eV to 285.5 eV (determined by peak fitting). This shift in peak position is

consistent with transformation of the carbon sp^2 bonding environment of between disordered to graphitic structure in the coating [57, 58] these values are reported in Table 3.1. The $1s$ to σ^* transitions begin around 288-289 eV and arise from $C1s$ transitions at C-C, C=C, and $C\equiv C$ bonded sites to unoccupied σ^* states [59]. The disordered nature of the coatings tended to spread the features of the σ^* resonance from 289-310 eV, but the characteristic diamond second band gap is clearly visible, and maintained the same overall shape, for all samples.

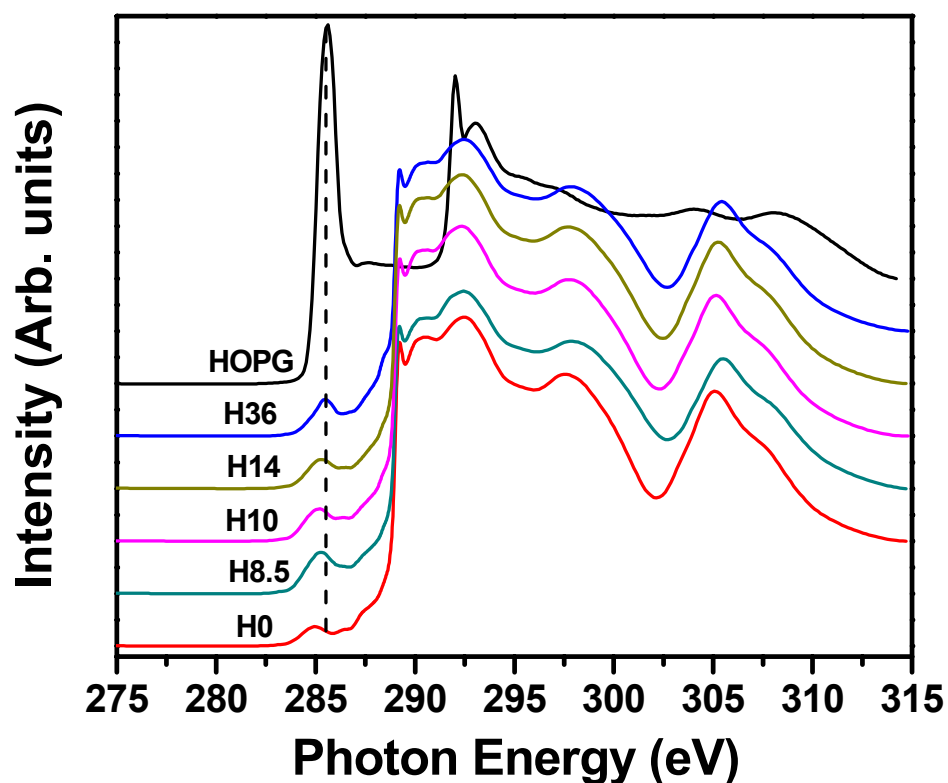


Figure 3.4 – NEXAFS scans for samples H0, H8.5, H10, H14, H36 and a graphite standard used in data reduction. The scans show the diamond exciton at ~ 288.5 eV and the diamond 2nd band gap at ~ 303 eV.

Chemical bonding composition analysis was carried out by a method described by Lenardi, et al [56]. The ratio of the peak areas of the 1s to π^* resonance to a large part of the 1s to σ^* portion of the spectra is compared to the same ratio in the pure graphite sample. Here the π^* peak, (the area under the curve from 282-288 eV) was compared to 288-310 eV in the σ^* portion of the spectrum. This method determines the contribution of the sp^2 bonded carbon in the sample. The sp^2 fraction is determined using:

$$f_{sp^2} = \frac{I_{sample}^{\pi^*} I_{HOPG}(\Delta E)}{I_{HOPG}^{\pi^*} I_{sample}(\Delta E)} \quad (17)$$

where $I_{sample}^{\pi^*}$ and $I_{HOPG}^{\pi^*}$ are the areas of the π^* peak, evaluated from 282 – 288 eV, of the NCD sample and the HOPG reference, respectively. $I_{sample}(\Delta E)$ and $I_{HOPG}(\Delta E)$ terms are the areas evaluated from over a large area of the spectrum, 288 eV – 310 eV [58]. The calculated sp^2 percentages for the coatings studied are listed in Table 3.1.

Of interest, is the composition and sp^2 content of these coatings. Qualitative line shape and sp^2 content of the recorded NEXAFS scan lines of the films studied compare with other reported data for NCD. The sp^2 content has been reported to vary from 5 to 30% [60]. Due to the changing growth environment, it was expected that the sp^2 character will change with growth conditions. Coating H0, grown in methane diluted in argon, had the lowest sp^2 fraction of 11%, while H90, which was grown in methane diluted in hydrogen, had the highest sp^2 fraction of 21%. Excepting sample H8.5, there is a trend, which can be seen in Table 3.1, of increasing sp^2 content with increasing H#.

3.5 Transmission Electron Microscopy

The TEM sample preparation and microscopy studies were conducted by R. McLellan and T. Biggerstaff [1].

The nanocrystalline diamond structures grown on silicon substrates were studied using High Resolution Transmission Electron Microscopy (HRTEM), Scanning Transmission Electron Microscopy (STEM), and Electron Energy Loss Spectroscopy (EELS). Using these techniques the microstructure and chemical composition of the NCD coating was determined. The films were prepared using Focused Ion Beam (FIB) thinning to achieve samples with a thickness of approximately 100 nm. EELS results allowed correlation between sp^2 and sp^3 bonding areas with intensity in Z Contrast images from the STEM studies. The areas of the film nearest to the surface are mostly sp^2 bonded, while the remaining bulk is sp^3 bonded. The graphite-like bonded carbon at the surface acts as a solid lubricant which could explain the good friction behavior seen in the tribology studies. Examination of wear track specimens after friction testing supports this conclusion.

From the HTEM images it is possible to determine grain size for the individual “diamond crystals” in the coatings. Figure 3.5 is a representative image that shows ~5-10 nm grain domains with little to no grain boundaries. This is consistent with other NCD samples in the literature.

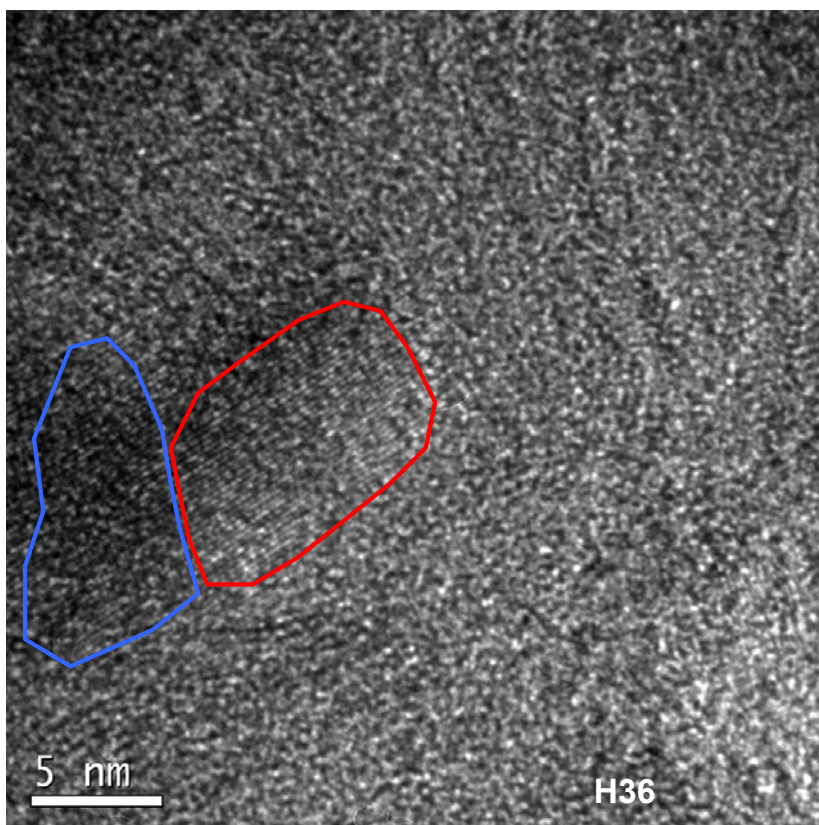


Figure 3.5 – H36 a representative TEM sample showing two in phase diamond grains, highlighted blue and red.

The EELS data also show that there is more sp^2 bonded carbon at the surface of the samples and in between the larger morphology structures than in the bulk. This could affect the sp^2/sp^3 ratios calculated from NEXAFS, as this is a surface technique. The sp^2/sp^3 ratio was calculated at ~1-5% from EELS and TEM techniques, Figure 3.6 shows bonding characteristics through a representative film. While not located between the grain boundaries, the sp^2 material (boxed in red) can also be in the areas between the larger morphologies at the surface.

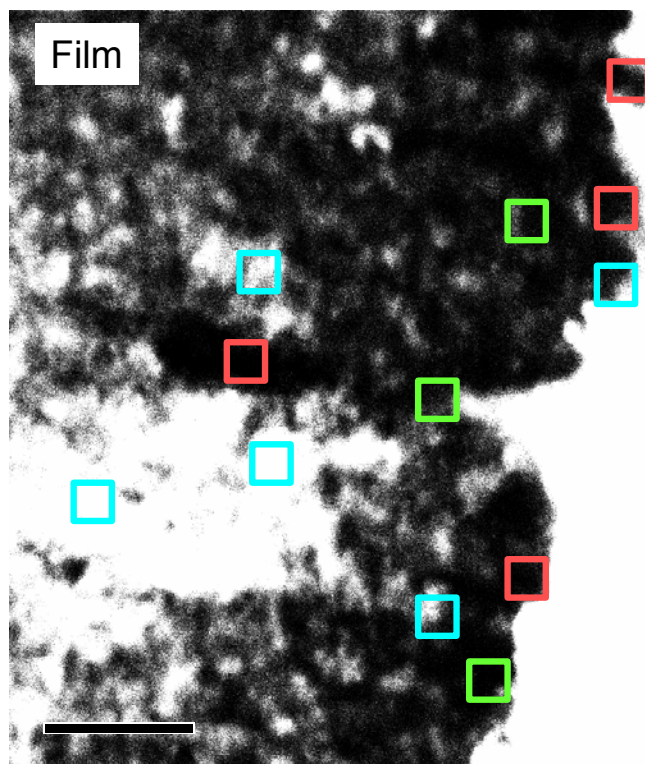


Figure 3.6 – A TEM EELS map image showing sp^2 (red), sp^3 (blue), and mixed (green) regions. The surface is on the right of the image and the scale bar indicates 10 nm.

3.6 Nuclear Scattering for Elemental Analysis

The Nuclear Scattering Measurements were carried out at Evans Analytical [61].

Nuclear scattering experiments were conducted at Evans Analytical. The measurements were made by placing a detector 30° from the forward trajectory of the He^{++} ion beam, and rotating the samples so that the incident beam strikes the surfaces 75° from normal, it is possible to collect light atoms, namely H, which are forward-scattered from the samples after collisions with the probing He^{++} ion beam. A thin absorber foil is placed over the detector to filter out He atoms that are also scattered from the sample. The experimental arrangement is shown in the accompanying figure. The H concentrations are determined by comparing the number of H counts obtained from reference samples after normalizing by the stopping powers of the different materials. An H implanted Si sample and a geological

sample, muscovite, were used as references for this analysis. The H concentration in the H implanted Si sample is taken to be its stated implant dose of 1.9×10^{17} atoms/cm². The muscovite (MUSC) sample is known to have ~6.5 atomic percent H and was measured at 6.9 % in this analysis.

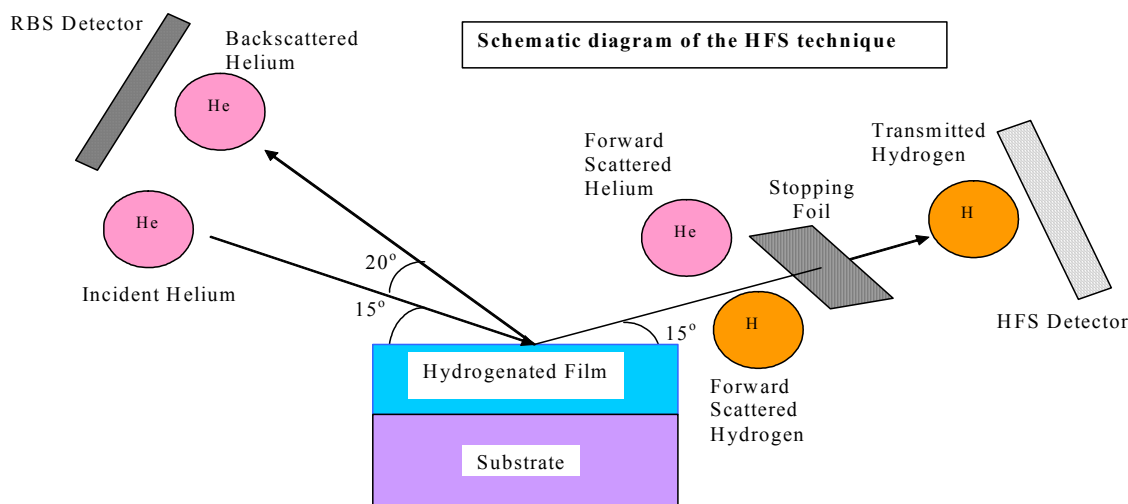


Figure 3.7 – Schematic of the scattering analysis experimental set up.

Data were acquired for charge accumulations of 5 and 40 μC . This is done in order to check for H modification in the analyzed region. Specifically, if H concentration is high in a film, diffusion of the H away from the irradiated area will occur. For 40 μC charge accumulations, the H spectra will indicate significantly less H than is actually present in the sample. A short charge accumulation (5 μC) provides a more accurate measure of the H concentration because H-loss is kept to a minimum. H modification was not observed on these samples. No modification of the samples was detected, so the samples were analyzed with the 40 μC charge accumulation.

Surface H due to residual hydrocarbon adsorption was taken into account by subtracting the H signal from a virgin Si reference sample from the H spectra obtained at the 30° detector for each sample.

Backscattering spectra were also acquired at an angle of 160° during the forward scattering sample orientation. These spectra are used to normalize the total charge delivered to the sample. The forward scattering spectra are fit by applying a theoretical model and iteratively adjusting elemental concentrations until good agreement is found between the theoretical curves and the respective experimental spectra. The simultaneous fitting of normal and grazing detector assists in generating a theoretical model that is representative of the physical structure of the sample.

Listed in the tables below are the theoretical models used to describe the samples. Due to the use of the He absorber foil, the H depth resolution is roughly 300Å so sharp variations in the H concentration may not be detected. There is an uncertainty of ±10% in the absolute H concentrations. The uncertainties in the concentrations of other elements are listed in Table 3.5. Detection limits are also listed for those elements not included in the theoretical models.

The forward scattering geometry cannot distinguish between lighter elements on the surface and heavier elements beneath the surface. This could cause confusion in the identification if it is based solely on the forward scattering spectra. Backscattering measurements with two detector angles is needed to uniquely determine the identity and depth of the higher Z elements in the films.

There is an uncertainty for layer thickness determined by backscattering because they are calculated using assumed film densities. The densities used to determine film thickness are included in the tables below. In general, the physical thickness of films should be checked with a direct measurement technique (SEM, TEM, AFM, profilometry). If the thickness of the films is known, the real density can be calculated. The equation governing the conversion from the backscattering densities and thicknesses and real thicknesses to the real densities is: $D_{\text{real}} = (D_{\text{BS}} \times T_{\text{BS}})/T_{\text{real}}$.

Table 3.2. H90 Analysis and Elemental Content

Depth (Å)	Atomic Concentration			Density (cm ³)
	H	C	O	
< 2000	5.5	93.5	1.00	1.13E23
2000 - 4000	4.7	94.3	1.00	1.12E23
> 4000	3.9	95.1	1.00	1.12E23

Table 3.3. H36 Analysis and Elemental Content

Depth (Å)	Atomic Concentration				Density (cm ³)
	H	C	O	Si	
< 700	8.8	90.6	0.50	0.100	1.12E23
700 - 1200	5.6	94.2	0.20		1.12E23
> 2100	4.1	95.7	0.20		1.12E23

Table 3.4. H0 Analysis and Elemental Content

Depth (Å)	Atomic Concentration				Density (cm ³)
	H	C	O	Si	
< 500	9.5	89.5	0.80	0.20	1.13E23
500 - 1000	7.6	92.2	0.20		1.13E23
> 1000	6.0	93.8	0.20		1.13E23

Table 3.5. Error and Tolerance in RBS Analysis and Elemental Content

Element	Uncertainty (at %)	Detection limit (at %)
Si	±0.5	0.5
O	±4	6
C	±6	6
H	±1	0.05

3.7 Summary of Characterization and Analysis

In summary, as the hydrogen content in the growth plasma was increased: coating RMS roughness increased, diamond grain size estimated from x-ray diffraction remained approximately constant, the intensity of the (002) graphite peak in XRD increased, the C 1s→ π^* peak position shifted from 285.0 eV to 285.5 eV and the preferred crystalline orientation of the coatings changed from diamond (110) to diamond (111). Also, sp^2/sp^3 ratio generally increased with increasing hydrogen content in the growth environment. The sp^2 content appears from TEM studies to be concentrated near the surface of the samples. Hydrogen content of the films was low, 5-9%, as expected for films of this type. The composition of the UNCD and NCD films discussed here and their relationship to other carbon films is illustrated in Figure 3.8. Nanocrystalline diamond and ultra-nanocrystalline diamond films are largely composed of sp^3 bonded carbon, but have some sp^2 carbon and hydrogen incorporated in the grain boundaries. This composition separates them from other coatings.

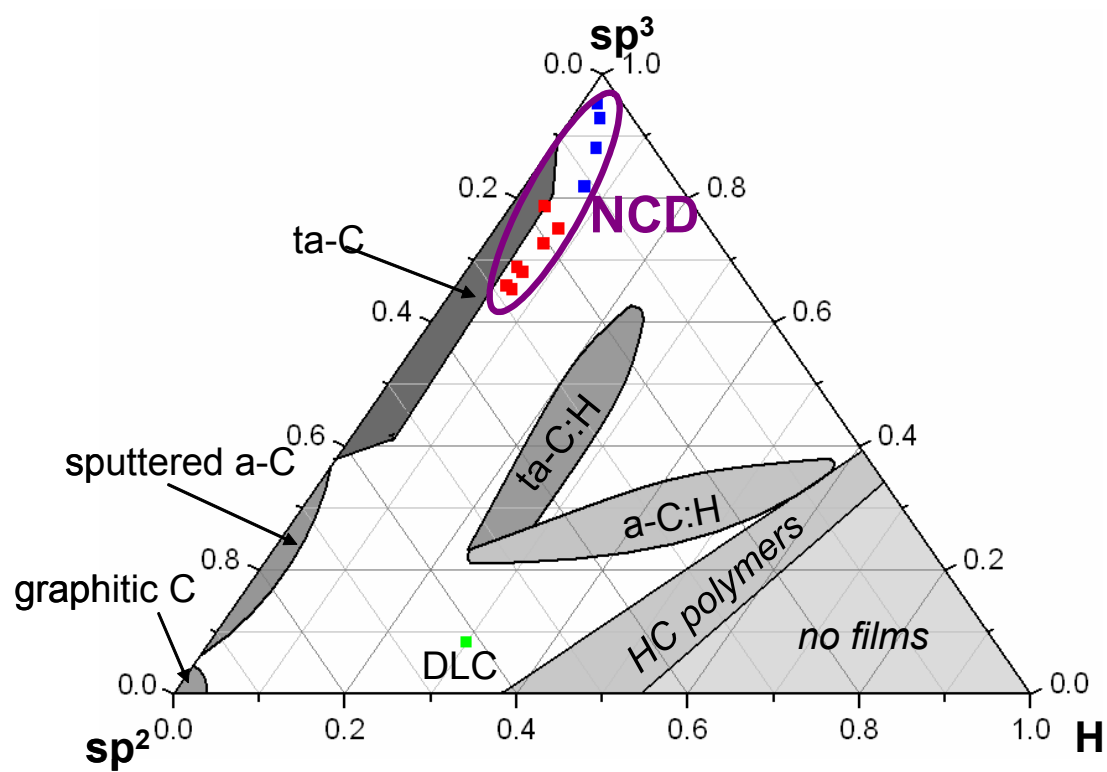


Figure 3.8 – Ternary diagram showing different carbon coatings and their $sp^3/sp^2/H$ content. The films discussed in this thesis fall in the purple oval marked NCD.

4. Plasma Characterization by Optical emission Spectroscopy

Optical emission spectroscopy is a non-intrusive diagnostic technique that can identify chemical species in the discharge by matching emission lines/bands to their source atom or molecule. It provides a measure of the plasma parameters, electron kinetic temperature T_e and electron number density n_e . A plasma is quasi-neutral and the number electron number density equals to the total ionic number density, $n_e = \sum_j Z_j n_j$, for all j -species in the plasma [33]. Electron plasma temperature and number density could be obtained from the spectra as described in the sections below.

4.1 Electron Plasma Kinetic Temperature

The intensity of emitted line is given by

$$I_{mn} = A_{mn} g_n N \frac{E_m - E_n}{Q} e^{-\frac{E_m}{kT_e}} \quad (18)$$

where A_{mn} = transition probability (/s), E_m & E_n = upper and lower level state energies (J), g_n = statistical weight of upper state, N = species particle density ($/m^3$), T_e = electron plasma temperature (K), Q = partition function. The electron temperature is then given by

$$kT_e = \frac{E_{m1} - E_{m2}}{\ln \left(\frac{I_2 \lambda_2^3 g_1 f_1}{I_1 \lambda_1^3 g_2 f_2} \right)} \quad (19)$$

where f is the oscillator strength at given wavelength λ .

Thus, for plasmas in local thermodynamic equilibrium (LTE), the relative line technique using the ratios of atomic, ionic, or molecular line intensities determines the kinetic temperature. The method relies on generating a Boltzmann plot using the relative line

method: $\ln\left(\frac{\lambda I}{gA}\right) = C - \frac{E_u}{kT_e}$, where λ is the wavelength, I is the relative intensity, g the statistical weight of the upper level, A the transition probability, E_u the energy of the upper level, k is Boltzmann's constant, T_e the plasma electron kinetic temperature, and C is a constant. The temperature of the plasma is determined from the slope of a line constructed from the Boltzmann factor, $\ln\left(\frac{\lambda I}{gA}\right)$ versus the upper level energy E_u [62, 63].

For high pressure discharges, several hundred Torr, the plasma usually departs from complete thermodynamic equilibrium (CTE), and thus the relative intensity method cannot be used, instead the continuum of radiation is emitted from the discharge and a neutral bremsstrahlung method would be employed. Such discharges are dominated by electron-neutral collisions over electron-ion collisions. For vacuum discharges in the range up to 100 Torr the plasma still departs from CTE but it can still be at local thermodynamic equilibrium (LTE), so the relative method could be applied here [63].

4.2 Electron Plasma Number Density

In a discharge where hydrogen is the working gas, or there is a hydrogen fraction in the gas mixture, the broadening of the H_α line may be used to obtain the electron number density. Thus, using H_α line and determining the line broadening, one can obtain the number density. The FWHM of Stark broadening is given by: $w_s = 2.5 \times 10^{-10} \alpha_{nn} (n_e, T_e) n_e^{3/2}$, where α_{nn} is the reduced wavelength ($\Delta\lambda / E_o$) and n_e in cm^{-3} and

$\Delta\lambda = 2W \times n_e \times 10^{-16} + 3.5A(n_e \times 10^{-16})^{1/4}$, where A is the ion-broadening parameter, and

could be neglected for non hydrogen plasmas. The nominal density from measured width:

$$n_e = \left(\frac{FWHM_{true}}{w_{measured}} \right) \times 10^{23} \text{ m}^{-3} [63].$$

4.3 Experimental Setup for Spectroscopic Measurements

Microwave plasmas, known as wave-heated discharges, are close to LTE and thus the relative line intensity method would be applicable.

Since the plasma enhanced CVD system is a 1.5kW ASTeX 2.45 GHz microwave system, operating at a chamber pressure of 65 Torr with nominal power input of 900 W, it is expected that the electron plasma kinetic temperature T_e will be in the range of 3-5 eV and the electron number density will be in the range of 10^{16} - 10^{18} /m³ as shown in Chapter 1 [5, 8, 9].

Measuring plasma parameters via optical emission spectroscopy will provide the means by which the plasma composition at the plasma-substrate interface during the coating process will be determined, and the effect of plasma parameters on the deposition and quality of films will be better understood.

Measured plasma parameters could be used in a plasma model for the microwave discharge then coupled to a deposition model for the structure and morphology of nanocrystalline diamond films, which can be used as a prediction model to optimize the coating process.

Two Ocean Optics HR2000 fixed grating spectrometers are available for use to obtain the spectra of the microwave discharge during coating process. Both spectrometers are fitted with a 600 line/mm grating, 25 μ m slit and Ocean Optics L2 internal lens to focus the light onto the CCD. The grating of the UV-VIS spectrometer is blazed at 500 nm and views the

wavelengths between 300 nm and 736 nm. The VIS-NIR spectrometer has a range of 600 nm to 1025 nm with the grating blazed at 750 nm. The spectrometers are power calibrated using an Ocean Optics LS-1-CAL lamp. A simplified drawing, Figure 4.1, shows the arrangement for optical emission spectroscopy measurements using a fiber optic bundle and the two spectrometers.

Spectral data to be transferred from the two spectrometers to a PC via IEEE interface card and an Ocean Optics software package. Collected spectral data will be analyzed using PeakFit spectra package to determine the emission, and/or absorption lines. Plasma composition will be determined and plasma parameters can be obtained.

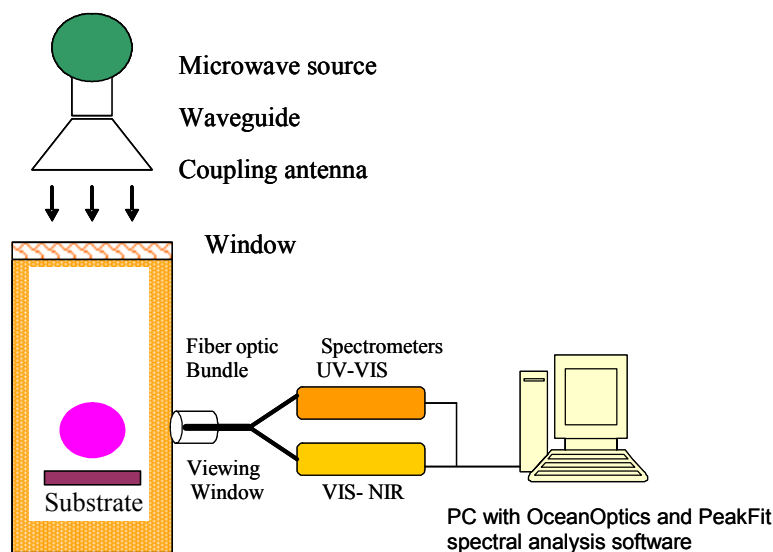


Figure 4.1 – Simplified diagram showing the experimental arrangement for emission spectroscopy, fiber optics pointing close to the surface of the substrate.

As the gas mixture is composed of $H_2/Ar/CH_4$, several collisional processes are expected and numerous spectral lines should be observed. Dissociation of molecular hydrogen into atomic hydrogen by electron impact is imminent:



(20)

Also ionization of molecular hydrogen and atomic hydrogen is expected



Dissociation of CH₄ is also expected



It is also to be expected to induce dissociation of CH₄ into carbon atoms and hydrogen release



and thus electron collision with carbon atoms may ionize carbon, and hence carbon spectral lines might also be seen



These reactions [5, 8] require very high energy input to the plasma and will not be seen here.

Abstraction reactions due to heavy particle collision can produce dissociation of molecular species and initiate radical formation such as the reaction:



This reaction is important in PECVD deposition.

Many studies were completed and are well documented in the literature [9, 10, 64], on diamond thin film deposition using methane in PECVD microwave discharges, as well as other plasma discharge systems. Through out these studies and this thesis, electron plasma temperature and number density are consistent. Typical values reported in the literature for electron kinetic temperature varies between 2 – 5 eV for 800 – 900 W microwave input power plasmas at pressure ranges 60 – 150 Torr. Electron number densities are within the

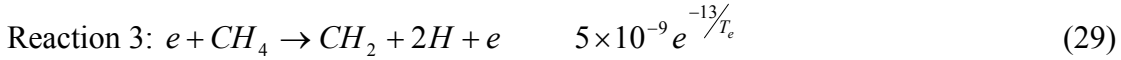
range of $10^{18} - 10^{19} /\text{m}^3$. It is also reported by May et al that for their 800 W 1% CH_4 / 2% H_2 / 97% Ar plasma at 100 Torr that the luminous plasma ball was roughly spherical about 2.5 cm in radius and position about 1 mm above the substrate [10]. In this work the plasma ball is also near spherical, about 2.5 cm in radius, and appears to hover just above the substrate surface.

4.4 Experimental Measurements

Optical emission spectra of the discharge at various gas mixing ratios were taken in both UV-VIS and VIS-NIR. The background spectra were taken to correct for the discharge spectra. For all obtained spectra, the background was taken in the UV-VIS and VIS-NIR and was subtracted for each corresponding spectra. The spectra was also taken for a pure hydrogen discharge at 900 W microwave power, system tuning allowed for 897 W forward power and only 3 W reflected, thus providing almost all power for ionization and electron heating. The spectra of the pure hydrogen discharge have shown the distinctive $\text{H-}\alpha$ (656.281nm) and $\text{H-}\beta$ (486.133nm) lines, which are due to neutral species.

4.5 Methane Plasma Description and Model

Reaction rate constants for electron impact collision in CH₄ discharges can be expressed by the following second order reactions, noted as reaction 1, 2, 3 and 4 [5], respectively; with the corresponding equation of reaction rate for each one:



These equations for reaction rate coefficients are used to obtain the variation in each reaction rate as a function of electron plasma temperature to determine which reaction, and consequently which mechanism, dominates for the microwave discharge used for PECVD of nanocrystalline diamond thin films. Electron plasma temperature is varied between 0.1 – 7.0 eV and Figure 4.2 shows the variation of reaction rate constants as a function of electron plasma temperature.

As seen in the figure, reaction 1 ($e + CH_4 \rightarrow CH_3 + H^-$) peaks at 4.7eV then decreases with electron temperature, suggesting that fewer negative hydrogen ions are produced as electron temperature is increased. This means the electrons are more energetic and therefore fewer are captured by hydrogen atoms. Reaction 2 ($e + CH_4 \rightarrow CH_3 + H + e$) is a mechanism by which CH₄ dissociates to CH₃ and a hydrogen atom. The rate constant for this reaction

increases with plasma temperature indicating that as expected, more molecules are dissociated as the plasma becomes more and more energetic.

Reaction 2 is important in the deposition of diamond thin films as it produces radicals (CH_3) that are an essential species in deposition of diamond films. In the other reactions, reaction 3 ($e + \text{CH}_4 \rightarrow \text{CH}_2 + 2\text{H} + e$) and reaction 4 ($e + \text{CH}_4 \rightarrow \text{CH}_3^+ + \text{H} + 2e$), the rate constant continues to increase with increasing electron plasma temperature indicating other dissociative processes and ionization are taking place, such as CH_3^+ in reaction 4.

To better understand the effect of each reaction, and the corresponding mechanism, reaction rate constants for the temperatures of 2, 3, 4, 5, and 6 eV are listed in Table 4.1, highlighting shows which reaction mechanism dominates at each temperature.

As seen in Table 4.1, reaction 1 is dominant at lower temperatures of 2 and 3 eV. This shows that the energy is not sufficient to induce ionization to positive hydrogen ions but is sufficient to dissociate CH_4 to CH_3 and a hydrogen atom. The weak dissociation electron is then captured by the excited hydrogen atom to form a negative hydrogen ion.

It can be seen in Figure 4.2 that reaction 1 peaks at approximately 4.7 eV and reaction 2, which produces CH_3 radicals, has a high reaction rate constant at 4.7 eV. Other reactions also have high reactions rates at 4.7 eV. This peak temperature correlates well with optical emission spectroscopy measurements of electron plasma temperature for hydrogen and methane/hydrogen plasmas. Measured spectra have shown strong H_α and H_β lines. A Boltzman plot, calculated from Eq. (19), using the measured intensities of H_α and H_β lines was used to calculate electron plasma temperature, the plasma electron temperature from the slope of the Boltzman plot was found to be approximately 4.7 eV.

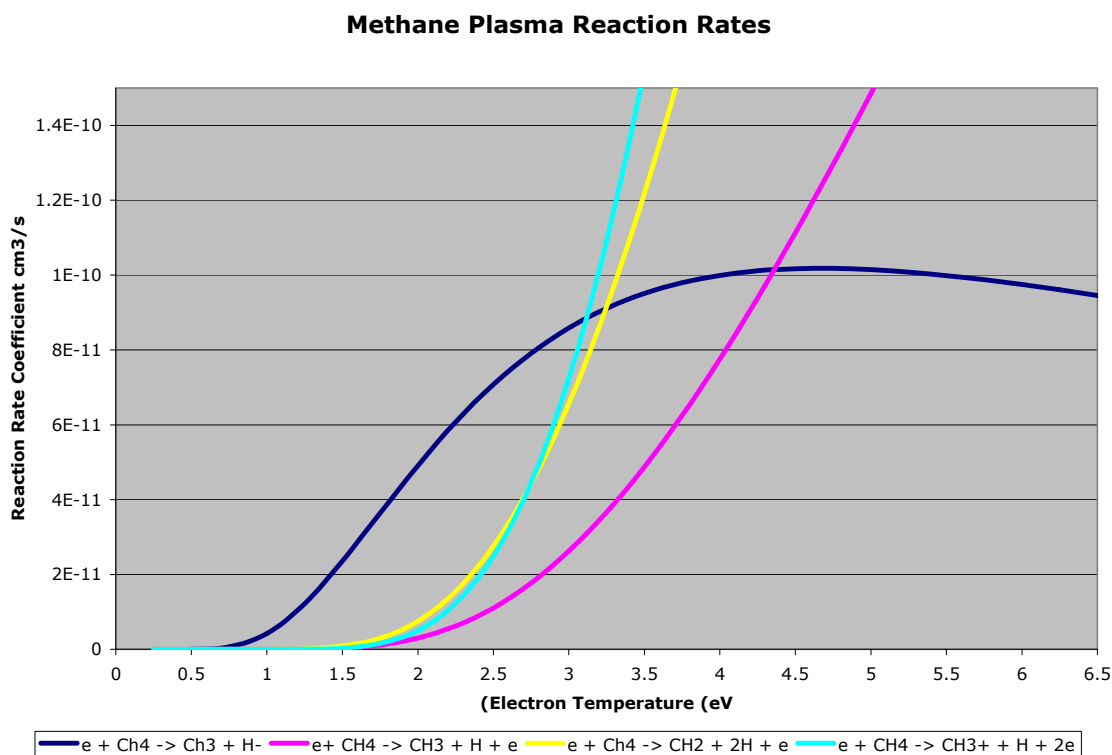


Figure 4.2 – Variation of reaction rate constants as a function of electron plasma temperature calculated from eqs. 29 – 32.

Further study of the data in Table 4.2 reveals that the reaction rates for reactions 1, 3 and 4 are comparable at a plasma temperature of 2 eV. However, once temperature increases to 3 eV only reactions 3 and 4 are comparable. Further increase in plasma temperature to 4 and 5 eV induces ionization of CH₃ and reaction mechanism 4 becomes dominant.

Table 4.1 – Second order reaction rate coefficients for methane plasma; (a) indicates the dominant reaction(s), and (b) similar reaction rates.

e + CH₄ → CH₃ + H⁻	e + CH₄ → CH₃ + H + e	e + CH₄ → CH₂ + 2H + e	e + CH₄ → CH₃⁺ + H + 2e	T_e
Reaction 1	Reaction 2	Reaction 3	Reaction 4	eV
4.91E-11 (a)	3.01E-12	7.52E-12	5.03E-12	2
8.58E-11 (b)	2.62E-11	6.56E-11 (b)	7.24E-11 (b)	3
9.99E-11	7.75E-11	1.94E-10 (a)	2.75E-10 (a)	4
1.01E-10	1.49E-10	3.71E-10	6.11E-10 (a)	5
9.75E-11	2.29E-10	5.73E-10	1.04E-09 (a)	6

The electron impact reactions 1-4 are the most probable reactions for electron impact in methane discharges. In order to weigh the effectiveness of a reaction over the others it was assumed that the above four reactions are the only reactions for electron impact in the methane discharge; one can assume that the sum of all reaction rate constants at each plasma temperature is the full (100%) reaction constant. These calculations are within the range of 4-6 eV (Table 4.1) and are consistent with Yamada's model and the values obtained from optical emission spectra. Electron impact on CH_4 that produces CH_3^+ is a reaction that takes place inside of the plasma ball; however it is followed by recombination of CH_3^+ with an electron to form a CH_3 radical. Therefore the ion behavior inside of the plasma directly correlates to abstraction and radical formation at the surface of the substrate.

Given this simplification a calculation of the percentage of each reaction rate constant with respect to the total of reaction rates would indicate the percentage contribution of each reaction mechanism at each specified plasma temperature. Table 4.2 shows the percentage contribution of each reaction in the methane plasma.

Table 4.2 – Percentage of each reaction in the methane plasma modeled in this thesis.

Reaction 1	Reaction 2	Reaction 3	Reaction 4	T_e (eV)
76	5	12	8	2
34	10	26	29	3
15	12	30	43	4
8	12	30	50	5
5	12	30	54	6

As seen from Table 4.2, reaction 1 dominates at low plasma temperature, approximately 2 eV. This reaction contributes 76% thus; the production of negative hydrogen ions is at its maximum. When the electron plasma temperature increases to 3 eV, production of negative hydrogen ions, reaction 1, drops to 34%. At this temperature production of CH₂ radicals from reaction 3, which are associated with an abundance of hydrogen atoms, rises to 26%. Also, production of CH₃⁺ ions and hydrogen atoms from reaction 4 increases to 29%. Increase of plasma temperature to 4, 5, and 6 eV boosts production of CH₂ to 30% and CH₃⁺ to 43%, 50%, and 56%, respectively. These conditions favor deposition due to both the availability of hydrogen atoms that promotes growth, and the availability of molecular ions and radicals, i.e. CH₃⁺ and CH₃, to deposit on the substrate. Given these conditions the production of radicals at 5 eV is 43% and ionic species 50%, a very favorable situation for deposition of carbon on a substrate. Spectral analysis of the discharge reveals that the plasma temperature is approximately 5 eV for a 900 W microwave plasma.

At an electron ion temperature of 2.5 eV, the ionization reaction for the production of CH₃⁺ and H⁺ can be compared to the production of radicals; the ionization fraction for H⁺ is about a factor of 3 greater than that of CH₃⁺ ionization. Ionization fraction is calculated using equations 31 and 32:

$$\text{Ionization Fraction } H^- = \frac{\text{rxn } 1}{\text{rxn } 2 + \text{rxn } 3} \quad (31)$$

$$\text{Ionization Fraction } CH_3^+ = \frac{\text{rxn } 4}{\text{rxn } 2 + \text{rxn } 3} \quad (32)$$

The model of plasma behavior above holds for hydrogen/methane/argon plasmas. Once argon is added into the mixture, the plasma temperature changes some what. As can be seen in Figure 4.3 the addition of argon into the plasma mixture decreases electron ion temperature. This is to be expected with the addition of argon as it has a much higher atomic number (Z) than either hydrogen or carbon so it requires more energy to ionize.

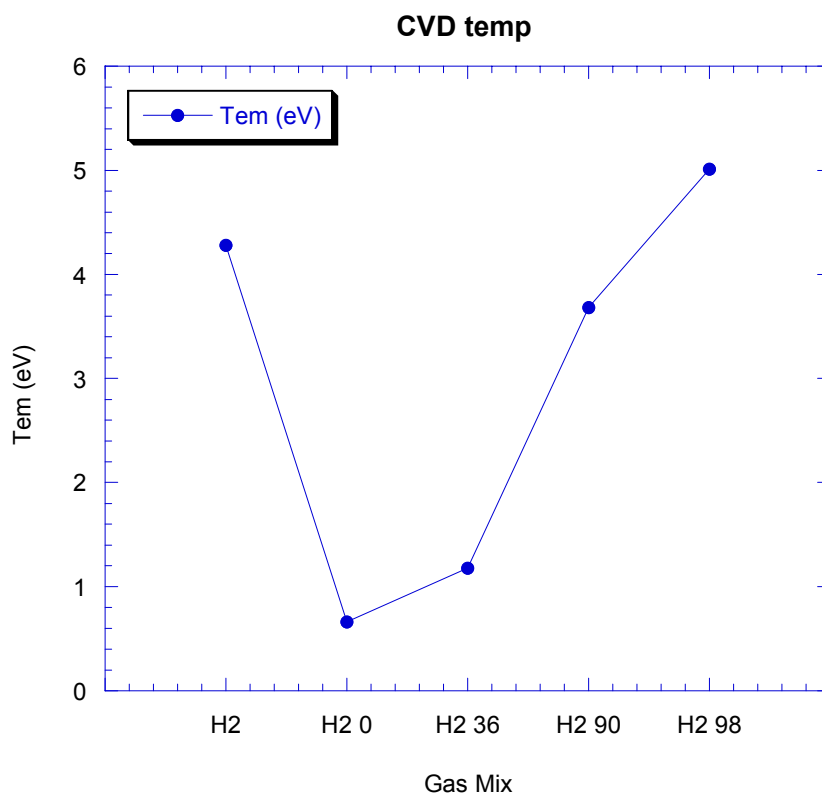


Figure 4.3 – CVD plasma temperature related to gas mixture. H₂ 90 indicates hydrogen makes up 90 % of the plasma. In all cases except H₂ and H₂ 98 methane is 10% of the plasma, hydrogen is as indicated and argon makes up the remaining part of the mixture.

Examining Figures 4.4 and 4.5, which are plasma UV and Visible spectra for the H36 plasma one can see many neutral and ionization lines. Most of these lines belong to carbon or hydrogen. There is one argon line evident in these spectra, 473.59 nm, however, this line is not a high intensity line in pure argon emission spectra. Lines for CH_x, with x = 1, 2, 3, or 4 are apparent in the plasma spectrum. These are the sources of carbon for growth of the films.

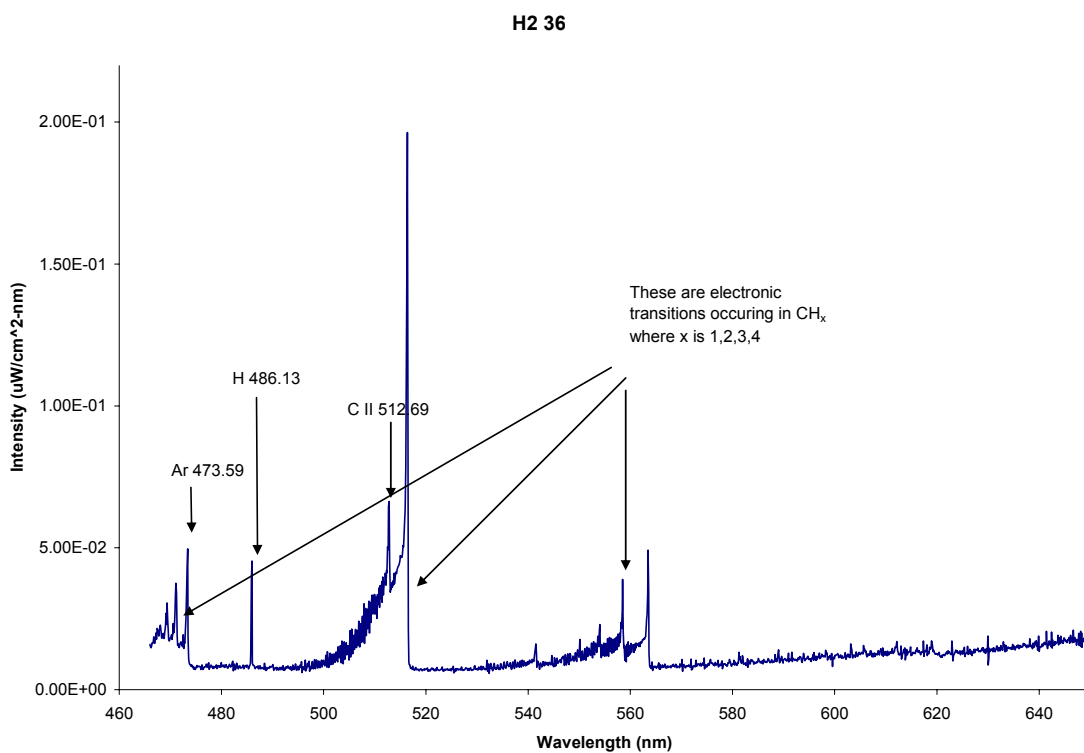


Figure 4.5 –Spectrum of a plasma with 10% methane, 54% argon, and 36% hydrogen.

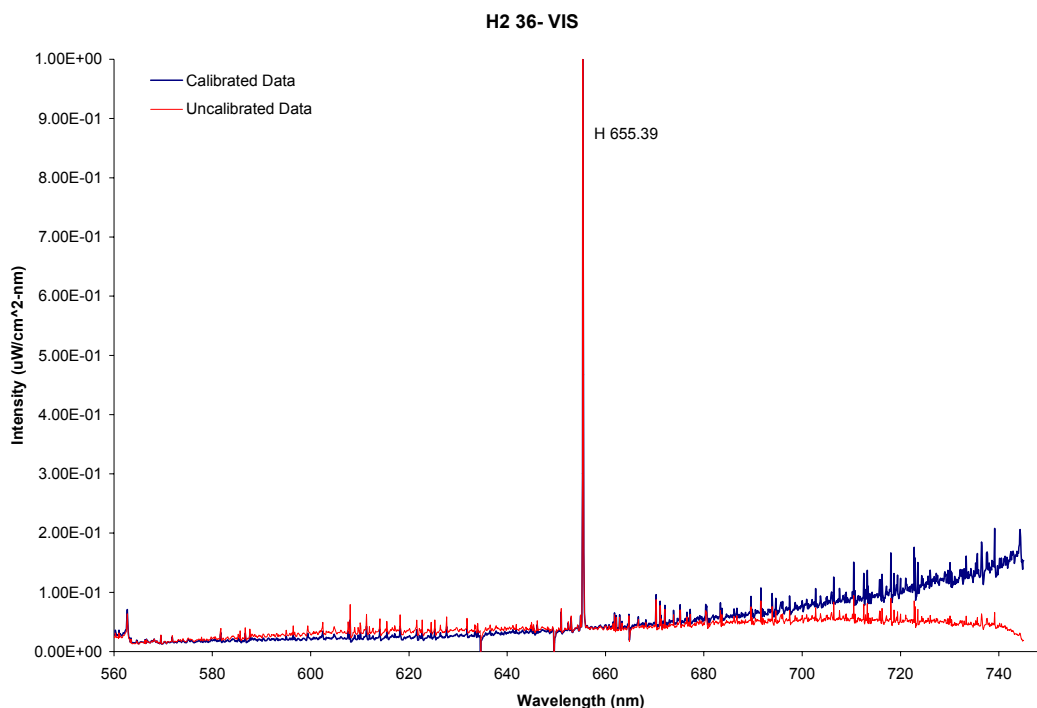


Figure 4.5 – Visible spectrum of plasma with 10% methane, 54% argon, and 36% hydrogen.

Looking particularly at the growth condition H98, we see that the application of a methane model to approximate plasma behavior is appropriate. This plasma, which contains 2% methane in 98% hydrogen behaves as one would predict from Figure 4.2. Its temperature is 4.7 eV, which is expected from the model used in Figure 4.3.

4.6 Summary of Plasma Characteristics

Approximating the behavior of argon/hydrogen/methane plasmas used for PECVD of nanocrystalline diamond on silicon gives insight into the usefulness and success of this growth method. The conditions needed for diamond deposition are creation of carbon radicals and ions to form the film and the correct ratio of species to promote polymerization (i.e.

growth) rather than etching of the substrate. Examination of these plasmas shows that this is indeed the case. Further, the growth conditions are optimized to promote growth.

Investigation of the reaction rate coefficients for dominant second order methane reactions at the electron plasma temperature for each set of deposition conditions show that reaction mechanisms for the creation of CH_3^+ ions and radicals dominate. These are the preferred reactions for deposition of nanocrystalline diamond films.

5. Tribology Studies of Nanocrystalline Diamond Coatings

Tribology studies were conducted at the Naval Research Laboratory with Drs. R. Chromik and K. Wahl. This chapter is an extraction of a manuscript submitted to WEAR for publication [66].

5.1 Reciprocating Sliding Tribology of Nanocrystalline Diamond Coatings

5.1.1 Experimental Setup and Measurements

Reciprocating sliding tests were conducted using a custom-built in situ tribometer [24, 65] designed to operate underneath an optical microscope. Direct observation of the contact region was conducted for all tests by using a transparent sapphire counterface. A 6.35 mm diameter sapphire hemisphere was loaded against a nanocrystalline diamond coating via a fixed load on a lever arm. The normal load on the coating was 6.4 N and resulted in an initial average Hertzian contact stress of 0.7 GPa. Friction tests were performed at room temperature in humid air (35-45% RH) up to 1500 cycles. All tests were run at a sliding speed of 1 mm/s over an initial track length of 6 mm. As the test progressed, the track length was shortened to 4 mm at cycle 100.

The friction force was measured from a calibrated piezoelectric force sensor housed in the sample stage. Data acquisition was conducted such that spatially resolved friction was measured across the track at 20 μm intervals. Average friction coefficients for a given cycle were determined from the central 10 – 90% of the track length from the average friction force divided by the normal load. Steady state friction values are calculated by averaging the last 200 data points of a test. Average steady state values for a given coating are reported from the average among 3 tests conducted on that coating. A period of high friction (run-in) occurred at the start of each test. When the friction reached a low value, typically $\mu < 0.1$, the friction was constant or only gradually changing. Thus, the number of cycles for run-in was

determined by taking a derivative of the friction trace. The cycle number when the derivative became zero was taken as the point when run-in was complete.

Optical images of the sliding contact were captured through the sapphire counterface with a Nikon 20x ultra-long working distance (ULWD) objective. Video of the test was recorded to both S-VHS video tape and to the hard drive of a DVD recordable unit. Image captures presented here were taken directly from the digital recording of the test.

Measurements of the mean contact diameter were made with standard photo editing software; with the length scale calibrated using a 0.01 mm scale marker for optical microscopy. *Ex situ* measurements of coating wear tracks and counterface wear flats were conducted with stylus profilometry and non-contact profilometry. Wear track depths were measured with a Tencor P-10 stylus profiler with a 2 μm radius tip. Cross sectional wear areas were calculated by integrating the height profiles.

Sapphire hemispheres were examined with a white light interferometric profiler (Zygo Newview 5000) with a 50X Mirau objective. A 3D height image of the wear scar was examined for all tests. Wear scar diameters were used to calculate a wear volume for the removal of a spherical cap from the sapphire counterface [67].

The run-in behavior was different for each coating, but in all cases a low steady state friction of $\mu \sim 0.05$ was eventually reached. Table 2.8 lists the average cycles of run-in calculated from three tests on each coating. Sample H36 reached low friction most quickly, while sample H0 took the longest. Also, H0 did not always reach $\mu = 0.05$ in steady state. The steady state friction for the two other tests run on H0 reached 0.08 and 0.1 for the final steady state friction coefficients.

5.1.2 *Ex Situ* Analysis – Wear Tracks and Transfer Films

Wear tracks were examined by AFM, with selected tests also examined with contact profilometry. In general, wear tracks had a polished appearance (see Figure 5.1 (b-d)). The reciprocating sliding process wore away much of the needle-like and cauliflower-like morphology that was apparent in as-prepared coatings (Figure 5.1(a)). Coating H8.5 had an as prepared RMS roughness of 30 nm. Figure 5.1 shows the wear tracks on this coating after 1, 100 and 1500 cycles.

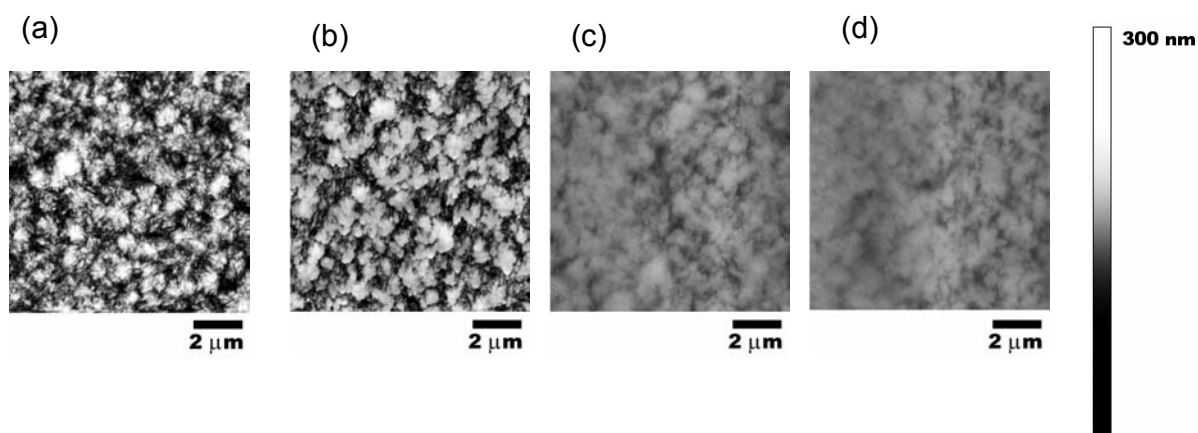


Figure 5.1 – AFM images of coating H8.5 : (a) as prepared coating and wear tracks at (b) 1 cycle, (c) 100 cycles, and (d) 1500 cycles.

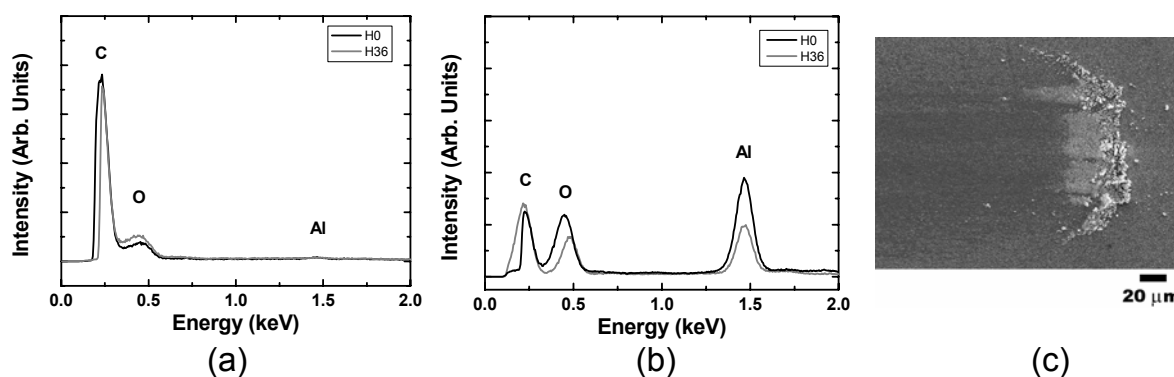
Even a single-pass track (see Figure 5.1(b)) exhibited smoothing of the coating and a slightly reduced RMS roughness of 26 nm.

Table 5.1 – Results for tribological performance of the nanocrystalline diamond coatings.

Sample	Cycles to Run-In	Steady State Friction	Wear Area (μm^2)	Counterface Wear Volume ($\times 10^3 \mu\text{m}^3$)	Cycles to Steady State diameter
H0	440 ± 100	0.05, 0.08, 0.1	3	27, 65, 71	50, -, -
H8.5	170 ± 30	0.049 ± 0.003	9	9 ± 5	50, 20, 50
H10	250 ± 30	0.046 ± 0.005	6	15 ± 2	30, 20, 50
H14	210 ± 50	0.055 ± 0.008	8	19 ± 2	20, 50, 50
H36	100 ± 50	0.048 ± 0.001	9	12 ± 5	20, 20, 20

Continued sliding resulted in lower RMS roughness values of 7.2 nm at 100 cycles and 6 nm at 1500 cycles. From Figure 5.2, it is apparent that most of the smoothing took place in the first 100 cycles. Worn track regions for all coatings after 100 cycles exhibited roughness on the order of 5 – 10 nm. Profilometry measurements of the wear tracks run for 1500 cycles revealed cross-sectional wear rates on the order of $10^{-6} \text{ mm}^3/(\text{N m})$ or less (see Table 5.1). Raw profilometry data indicated average wear track depths of no more than 50 nm for the coatings studied.

Chemical analysis of the wear tracks with EDS revealed a signal for aluminum both in the track and at the turn around points.

**Figure 5.2** – EDS data for (a) wear tracks on coating H0 and H36, and for (b) endpatches on H0 and H36 (c) SEM image of the endpatch on H36

Figures 5.2 (a) and (b) show the EDS data collected from two regions of a wear track on samples H0 and H36. Some evidence of aluminum is found in the track, but the majority of worn sapphire from the counterface was found as debris at the turn-around points. Thus, the smoothing of the coating observed in Figure 5.1, was due mostly to diamond polishing but also from some sapphire left in the wear track. Figure 5.2(c) shows the typical debris collected at the end of a wear track on coating H0.

Non-contact profilometry carried out on the sapphire counterfaces showed that a wear flat was generated by sliding against the diamond coatings. Figure 5.3 is a profilometry scan on a counterface run against coating H36.

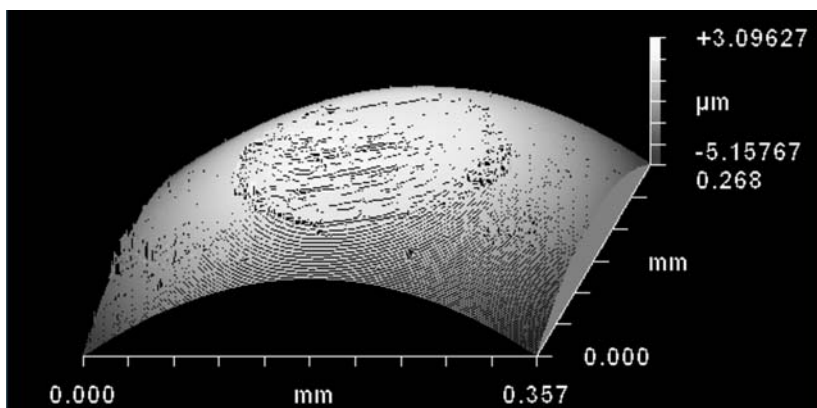


Figure 5.3 – Non-contact profilometry scan for wear scar on sapphire counterface run against H10.

A spherical cap of material was removed, whose volume was calculated from the diameter of this wear scar [67]. Table 2.8 lists average counterface wear volumes for testing against each NCD coating. Except for coating H0, the wear volume was similar for each of the three tests and an average is reported. For coating H0, the wear volumes differed significantly among the three tests, and were always higher than any individual measurement for the other coatings.

Ex situ Raman spectroscopy revealed evidence of a carbonaceous transfer layer on the sapphire counterfaces.

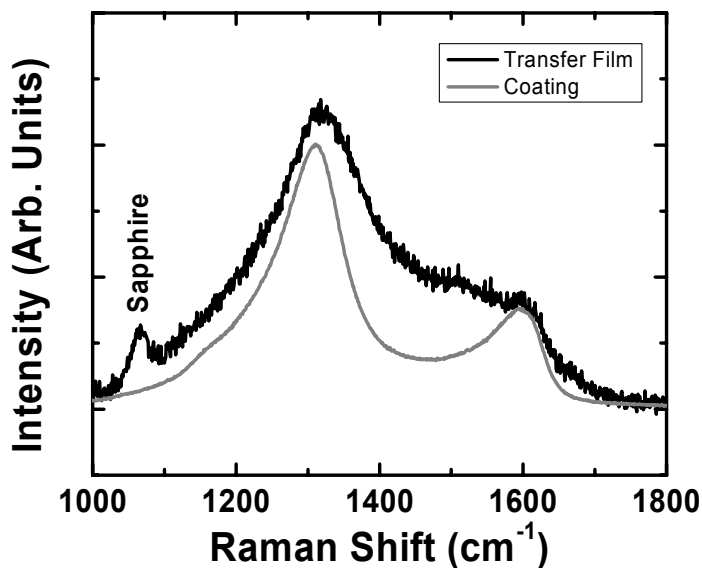


Figure 5.4 – Raman spectrum from coating H36 and from a transfer film on sapphire from a test run on this coating.

Figure 5.4 shows Raman spectrum (785 nm excitation) collected from the center of a wear scar for a test conducted on coating H36 and the spectrum from the as-prepared coating. The nature of the transfer film spectrum is qualitatively similar to the spectrum from the as-prepared coating. Similar spectra were obtained from the counterfaces used on other coatings. No evidence for an enhanced graphitic nature of the transfer film was found. In a study by Scharf, et al. [65] on diamond-like carbon coatings, a secondary G band at higher wavenumber was found and interpreted as evidence of graphitic transfer film formation. For this study, a change in excitation wavelength from 514 nm to 785 nm was necessary to reduce a strong fluorescent background signal. The wavelength shift also reduced the

sensitivity to the G band of carbon, possibly masking detection of a transformation to graphitic carbon [42-47]. From this Raman study of the sapphire counterfaces, we find that a carbonaceous transfer film forms that is similar to the parent NCD coating.

5.1.3 *In Situ* Observations

Examination of the sliding contact revealed that the contact diameter increased as the test progressed. Measurements of the contact diameter from an in situ image during the final sliding cycle correlated well with ex situ measurements by non-contact profilometry. Thus, the increase in the observed contact diameter was found to correspond directly to the wear of the sapphire counterface. Figure 5.5 contains plots of contact diameter, as well as friction coefficient, versus sliding cycle for coatings H0, H8.5 and H36.

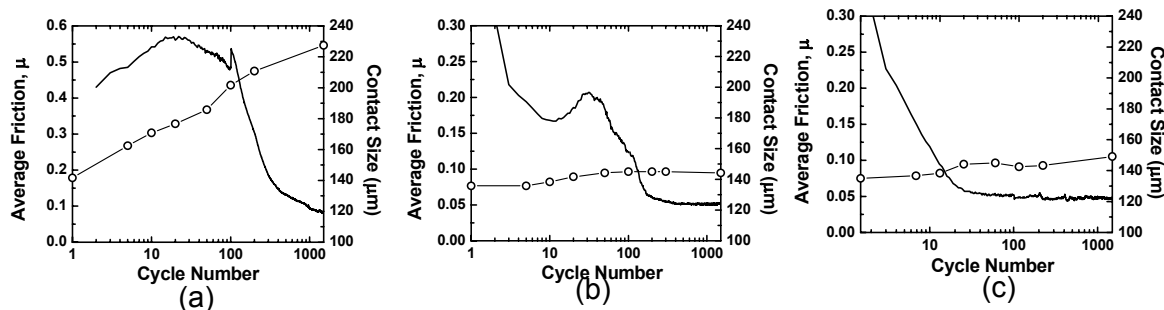


Figure 5.5 – Friction (solid lines) and contact diameter (open circles) versus sliding cycle (a) H0, (b) H8.5, and (c) H36.

For coating H0 (Fig. 5.5 (a)), the contact diameter steadily increased throughout the test. Based on these measurements, the average contact stress fell to roughly 0.2 GPa at cycle 1500. During this test, a friction coefficient of 0.05 was never attained and the steady state friction was 0.08. While the friction was high, the sapphire counterface was continually wearing, apparent from the steadily increasing contact diameter.

The other NCD coatings typically reached a low friction in fewer sliding cycles than the test in Figure 5.5(a) and correspondingly reached a steady state contact diameter more quickly. This is depicted in Figure 5.5(b) and (c) for coating H8.5 and H36, respectively. For coating H8.5, the contact diameter increased to 140 μm by cycle 50 and remained this size for the remainder of the test. This increase in contact diameter corresponded to a reduction in the average contact stress to roughly 0.4 GPa. A wear volume calculated from this in situ measurement, 6.6 μm^3 , corresponded well with what was measured *ex situ* (see Table 5.1). Similarly, for the test on coating H36, the contact diameter increased to 145 μm by cycle 20 and was constant in size for the remainder of the test. The wear volume from this measurement is 8 μm^3 , again in agreement with the *ex situ* results (Table 5.1).

Similar to the results presented in Figure 5.5 (b) and (c), most tests resulted in a rapid abrasion of the sapphire counterface (observed by an increase in contact diameter) followed by steady state sliding of a wear flat versus the NCD coating. This wear behavior was observed for all coatings and did not depend on the magnitude of the friction during run-in or how long run-in lasted (e.g. the run-in for H36 was minimal but the sapphire still wore). An exception was coating H0, where, for two tests, a low steady state friction of $\mu \sim 0.05$ was never reached. In these cases, as displayed in Figure 5.5 (a), the sapphire counterface wore throughout the test.

Observation of the sliding contact also allowed for determination of the velocity accommodation mode (VAM) [21-24]. Based on video imaging, no wear debris was observed to move within the contact region. However, *ex situ* Raman analysis identified that a carbonaceous transfer film does form. Based on these observations the VAM was found to

be interfacial sliding of a thin transfer film versus the NCD coating. Interfacial sliding is a low energy VAM that typically results in low friction, especially for solid lubricant materials such as DLC or MoS₂ [24, 65, 68, 69].

5.2 Pin on Disk Tribometry

5.2.1 Experimental Measurements

Tribology data were determined using a CSM Instruments Pin-on-Disk tribometer. Friction versus cycle number is plotted in Figure 5.6 for individual tests on the NCD Coatings.

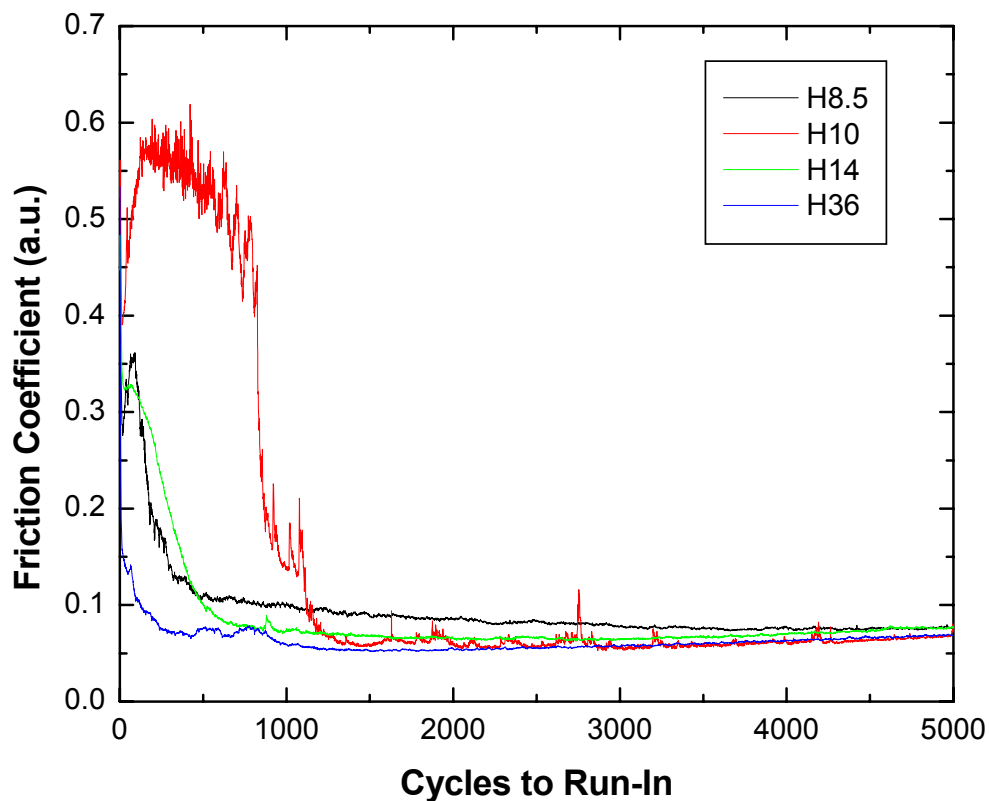


Figure 5.6 – A plot of friction versus cycle number for films H8.5, H10, H14, and H36.

Run-in behavior was different for each coating, but a low steady state value of $\mu = 0.06$ for H10 and H36 and $\mu = 0.08$ for H8.5 and H36 was obtained. Table 5.2 lists the cycles to run-in for each coating.

Table 5.2 – Cycles to run-in for Pin-on-Disk tribometry.

	Final Friction	Cycles to Run In
H8.5	0.8	500
H10	0.6	1500
H14	0.8	750
H36	0.6	450

For sapphire counterfaces sliding against nanocrystalline diamond coatings, low friction coefficients ($\mu \sim 0.07$) were observed after a run-in period of high friction. This result is different from previous studies of sapphire sliding against microcrystalline diamond (MCD) coatings where high friction was measured [32]. Friction performance of MCD can be enhanced by polishing, but does not achieve the low friction coefficients reported here [28]. The high friction run-in behavior found for these NCD samples has previously been observed for NCD coatings [20, 21]. Sliding Si-N against NCD exhibited high friction followed by $\mu \sim 0.1$ for humid conditions [20]. In a different study of self-mated NCD surfaces, high friction run-in was followed by a steady state friction coefficient as low as 0.02 [21]. The number of cycles to run-in was found to vary from sample to sample similar to our results.

5.2.2 Pin-on-Disk Friction Behavior and Performance

Figure 5.7 is a plot of the average number of run-in cycles versus coating roughness. Only a slight trend for run-in is found with coating roughness. Coating H36 has the greatest

RMS roughness and the shortest run-in. Other samples have similar roughness to each other, however, run in changes from sample to sample. It is apparent that factors other than sample roughness must contribute to the run-in behavior of these coatings.

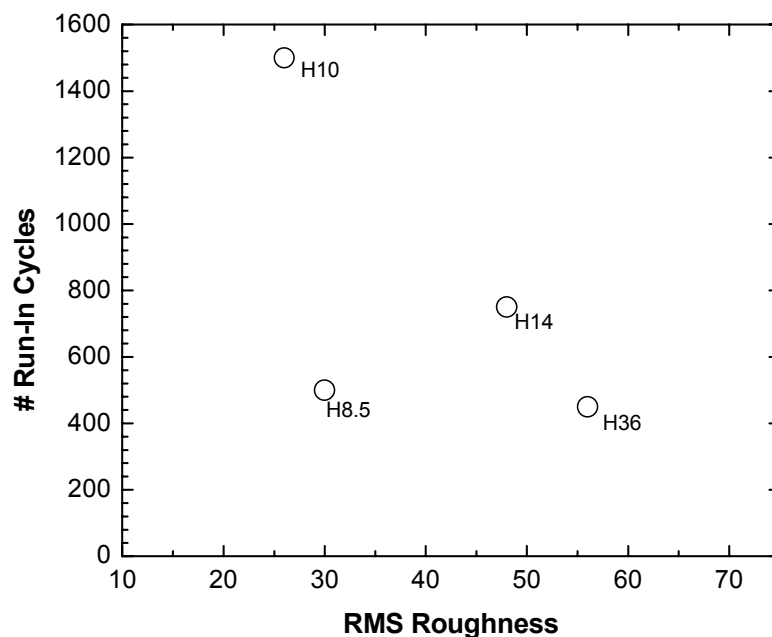


Figure 5.7 – RMS roughness versus cycles to run-in for samples H8.5, H10, H14, and H36.

Little correlation was determined between grain size and run-in behavior. Grain size measurements using x-ray diffraction have shown that all of the grain sizes are similar (Table 2.1). While grain size remained similar, a qualitative measure of grain orientation showed that coatings H8.5, H10, and H14 all have a (110) texture where as H36 has a (111) texture. Friction behavior of single crystal diamond varies with exposed crystal face, however, these samples are polycrystalline and do not display a strong orientation preference. No trend in behavior and performance is evident with film texture.

While run-in behavior was not correlated with roughness and orientation, it can be correlated with the intensity of the x-ray peak at 26° . This peak is consistent with the (003) reflection of graphite. Here it indicates sp^2 -graphite-like material that we have associated with the grain boundaries in these NCD coatings. The intensity of this peak varies across the sample set. A definite trend is found in run-in with the intensity of the grain boundary peak. A more intense 26° peak is accompanied by a shorter run-in period, as shown in Figure 5.8.

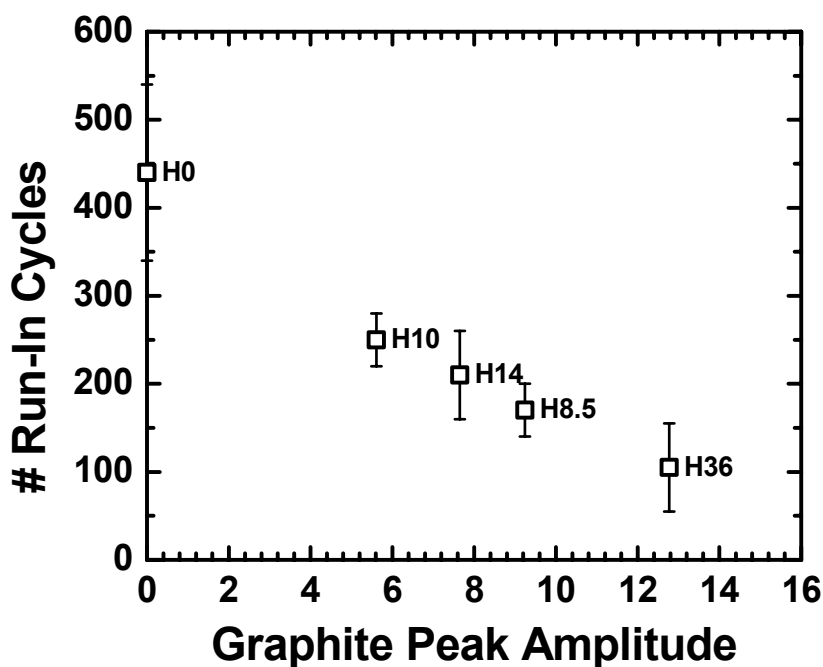


Figure 5.8 – Cycles to run-in plotted versus intensity of the 26° XRD peak intensity.

Based on these results, a small amount of graphite-like material in the grain boundaries apparently has a beneficial effect on the tribological performance of these coatings.

A trend with cycles to run-in and sp^2 content is observed, except H8.5, which had higher than expected sp^2 content and ran-in faster than expected. Run-in versus sp^2 content is shown in

Figure 5.9. These results suggest that a certain amount of sp^2 content in the NCD coatings is useful in eliminating run-in.

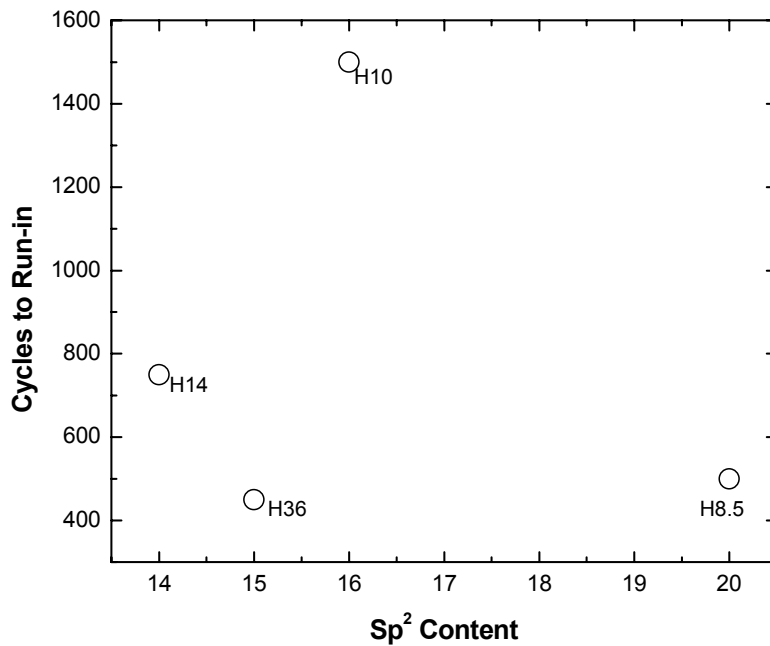


Figure 5.9. Cycles to run-in versus Pin-on-Disk friction coefficients.

6. Discussion

6.1 Tribology and Materials Characteristics

Tribology studies were conducted at the Naval Research Laboratory with Drs. R. Chromik and K. Wahl. The tribology discussion in this chapter is an extraction of a manuscript submitted to WEAR for publication [66].

For sapphire counterfaces sliding against nanocrystalline diamond coatings, low friction coefficients ($\mu \sim 0.05$) were typically observed after a run-in period of high friction. This result is different from previous studies of sapphire sliding against microcrystalline diamond (MCD) coatings. Bull, et al. [32] found that sapphire sliding versus MCD coatings ($40 \text{ nm} < Ra < 80 \text{ nm}$) always had high friction. Similarly, Hayward, et al. [29] found that rough diamond coatings never achieved low friction but highly polished MCD coatings ($Ra < 10 \text{ nm}$) ran-in quickly to $\mu < 0.1$. Similar to the two tests on NCD coating H0 from this study, both previous studies found that MCD coatings resulted in sapphire counterface wear throughout the test.

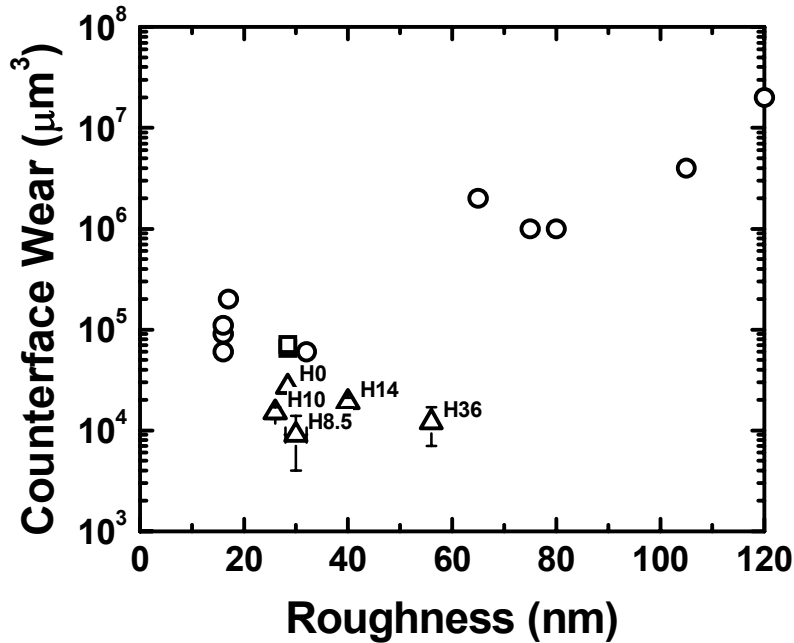


Figure 6.1 – Counterface wear versus diamond coating roughness. Open circles are from [29] with roughness (Ra) calculated from line profiles from contact profilometry. Open triangles are from this work with roughness (RMS) calculated from AFM scans. The square data points are for the two tests on H0 where the counterface wore continuously throughout the test.

Figure 6.1 is a plot of the volume of counterface wear versus the roughness of diamond coatings for both the study by Hayward, et al. [29] and the data collected here. For MCD samples, the counterface wear had a significant dependence on the initial roughness of the diamond coating. In contrast, for the five NCD coatings studied here, the amount of counterface wear was somewhat independent of coating roughness and was always less than was found for MCD coatings. For the two tests on coating H0 that had higher friction, the counterface wear was greater and more comparable to that found for MCD.

Because Hayward, et al. [29] used lower loads (5 N) and different sliding distances from our study, further interpretation of Figure 6.1 requires the calculation of wear rates:

$$WR = \frac{\text{Worn volume}}{\text{Load} \cdot \text{Sliding distance}} \left(\frac{\text{mm}^3}{\text{N} \cdot \text{m}} \right) \quad (33)$$

For our study, wear rates of the sapphire balls were on the order of $10^{-8} \text{ mm}^3/(\text{N m})$. When the ball wore continuously (two tests on H0), the wear rate was $10^{-6} \text{ mm}^3/(\text{N m})$. Hayward found higher wear rates, between 10^{-5} and $10^{-2} \text{ mm}^3/(\text{N m})$, for sapphire sliding against MCD. Bull, et al. [32] also found high sapphire wear rates between 10^{-5} and $10^{-4} \text{ mm}^3/(\text{N m})$. Thus, the NCD coatings studied here were found to have significantly different tribological behavior from MCD coatings. In most cases, the sapphire wear took place within the first 50 sliding cycles followed by interfacial sliding of a carbonaceous transfer film versus wear track with $\mu \sim 0.05$. This is a significant improvement in tribological performance as compared to MCD coatings and is possibly tied to the formation of the transfer film, a phenomenon known to aid in low friction and reduce wear [23, 24].

The high friction run-in behavior found for our NCD samples is a common feature of NCD coatings [20, 21]. Erdemir, et al. [20] studied Si-N sliding versus NCD and found regimes of high friction followed by $\mu \sim 0.1$ for humid conditions. Similarly, Abreu, et al. [21] studied self-mated NCD tribology and found high friction run-in followed by steady state friction as low as 0.02. For our specimens, the number of cycles to run-in was found to be different for each sample. In some cases, the run-in was very in comparison to what previous researchers have observed on NCD coatings.

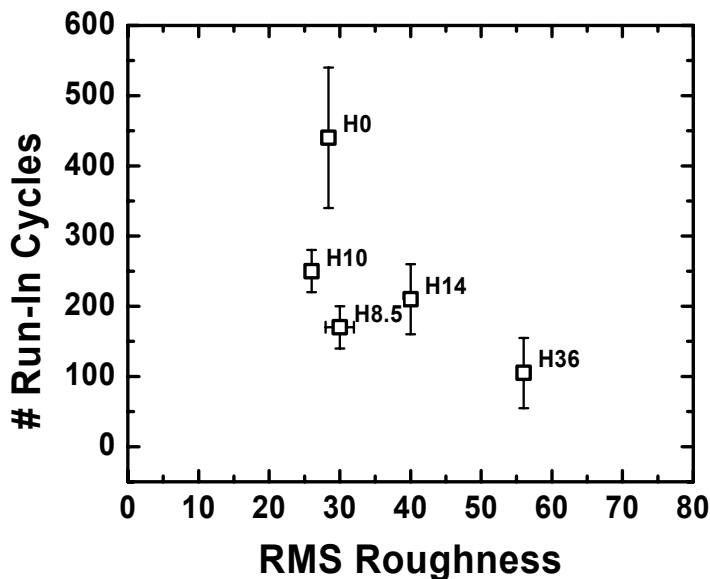


Figure 6.2 – Average number of cycles to run-in versus RMS roughness in reciprocating sliding tribometry.

Figure 6.2 is a plot of the average number of run-in cycles versus NCD coating roughness. Only a weak trend for run-in is found with coating roughness. Coating H36 has the greatest RMS roughness and the shortest run-in. The remainder of the specimens have virtually the same roughness (20 – 40 nm), but H0 has significantly longer run-in time. Thus, other factors were considered as contributing to the run-in behavior of NCD coatings.

From the x-ray diffraction studies, the grain size of both diamond and graphite crystallites for all coatings was found to be similar, but the diamond orientation and graphite content varied from sample to sample (see Table 2.1). Considering coating texture first, Figure 6.3 shows a plot of run-in cycles versus the ratio of the intensity of the diamond (111) peak to the diamond (220) peak measured from x-ray diffraction.

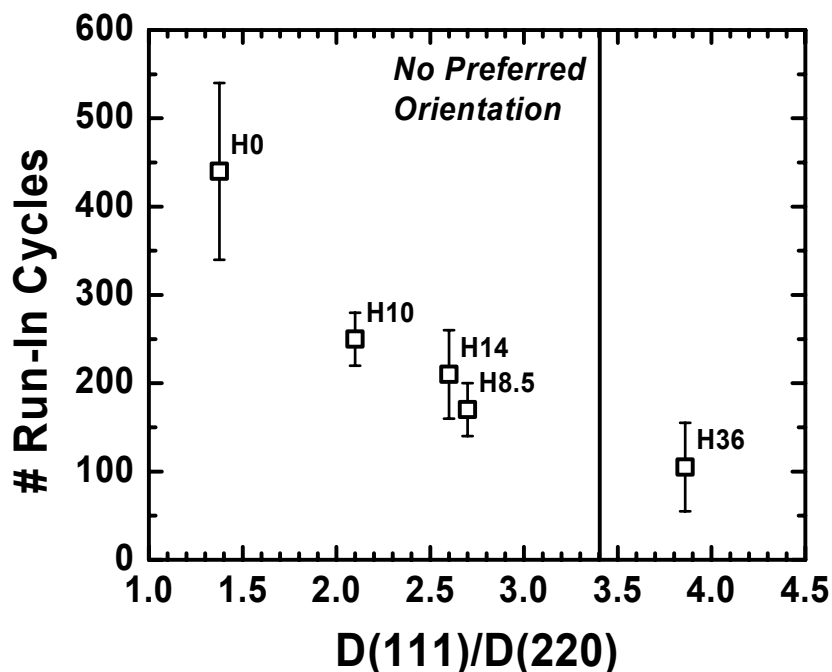


Figure 6.3 – Average number of run-in cycles versus diamond orientation.

A trend is observed of decreasing run-in as the preferred crystalline orientation changes from (110) to (111). The friction and wear behavior of diamond is known to be anisotropic with the exposed crystal face [27, 70, 71]. However, our NCD specimens are polycrystalline and the extent of texturing was found to be rather weak. Additionally, based on the work of Enomoto and Tabor [70], the friction anisotropy for diamond typically disappears below a critical contact stress of 20 GPa, a transition point much greater than our contact stress of 0.7 GPa. Therefore, despite the trend found in Figure 6.3, crystallographic texture of our diamond coatings is not a likely mechanism for the differences in the observed tribological behavior.

Coating chemistry may also play a role in the run-in behavior. A combination of the XRD and NEXAFS data was used to examine the state of the sp^2 bonded carbon in NCD coatings. From NEXAFS data, there was only a small variation in the *total* percent of sp^2 bonded carbon, but there was also a significant variation in $C1s \rightarrow \pi^*$ peak position. The total percent reflects both amorphous and crystalline sp^2 carbon while the shift in the peak position has been related to the structure of the sp^2 carbon, with amorphous carbon materials tending to have lower peak position relative to graphite [57, 58]. Figure 6.4(a) is a plot of the normalized amplitude of the graphite (002) peak from XRD versus percent sp^2 . The correlation of these two measurements is weak, with an $R^2 = 0.65$ for a linear fit. The (002) peak only corresponds to crystalline graphite, not amorphous. Figure 6.4(b) is a plot of relative graphite (002) peak amplitude versus the $C1s \rightarrow \pi^*$ peak position.

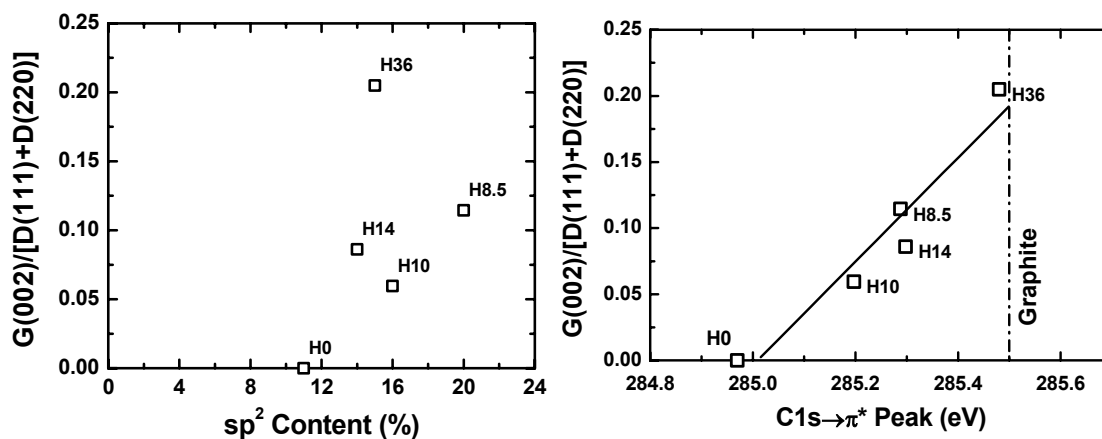


Figure 6.4 – Plots of the graphite peak (002) amplitude normalized to the sum of the diamond peak amplitudes [(111) and (220)] versus measurements from NEXAFS, including (a) the sp^2 content and (b) the position of the $C1s \rightarrow \pi^*$.

The coating with no discernable graphite by XRD showed C=C bonding at 285.0 eV, with shifts to 285.5 eV for the films containing increasing amounts of crystalline graphite. There is a linear relationship with $R^2=0.93$.

The XRD data reflects ordered sp^2 bonded carbon (graphite), while the NEXAFS $C1s \rightarrow \pi^*$ intensity reflects both ordered and amorphous sp^2 bonded carbon. The strong correlation between $C1s \rightarrow \pi^*$ peak position (but not intensity) with the XRD data is consistent with this interpretation. Interestingly, similar shifts to more graphite-like $C1s \rightarrow \pi^*$ peak positions have also been reported for a-CN films under varying growth conditions [72]. The detailed nature of what bonding configurations are responsible for the observed peak shift is not known. Gago et al. [58] suggest that this downshift in $C1s \rightarrow \pi^*$ peak position may be related to either disordered graphitic carbon or sp^2 pairs and/or chains. In our work, we find the $C1s \rightarrow \pi^*$ peak position to be correlated to the quantity of graphite crystallites (of a few nm in size) relative to the overall sp^2 content of the coatings estimated from the NEXAFS peak areas.

Figure 6.5(a) is a plot of the sp^2 content versus run-in cycles. A weak trend toward decreased run-in with increasing sp^2 content is found. Figure 6.5(b) is a plot of the normalized (002) graphite peak from XRD and $C1s \rightarrow \pi^*$ peak position from NEXAFS versus the number of run-in cycles.

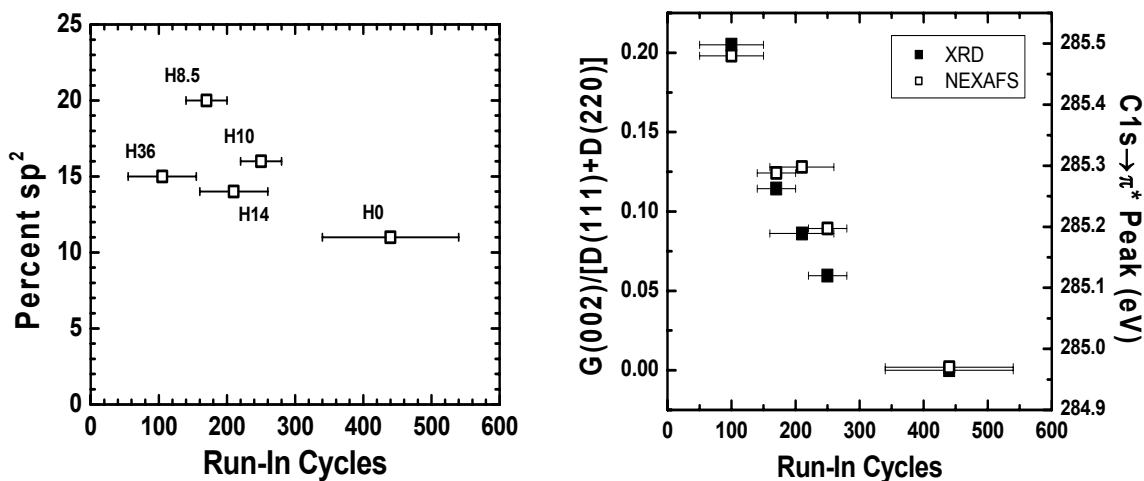


Figure 6.5 – Plots of coating properties from NEXAFS and XRD versus run-in cycles, including (a) percent sp^2 , and (b) normalized graphite peak amplitude and $C1s \rightarrow \pi^*$ peak position.

These results demonstrate a definite trend between run-in and the graphite content of the film. Sample H0, which had no graphite peak present, had the longest run-in and also had two tests where higher steady state friction and continuous wear of the sapphire counterface was observed. All other coatings exhibiting this graphite peak had shorter run-in and always exhibited low steady state friction. Sample H36, with evidence for the most graphite, had short run-in and in some cases a very quick realization of low friction (Figure 6.5).

The evidence presented here indicates that the degree of crystalline order of the sp^2 bonded carbon in the coating plays a role in the run-in friction behavior of NCD. Based on the current understanding of the structure of NCD [14] prepared by methods similar to those used here, sp^2 bonded carbon exists in the grain boundaries between diamond crystallites, but is typically structurally amorphous. For the coatings prepared here, certain growth conditions led to more order for the sp^2 bonded carbon and also resulted in more rapid run-in to low

friction. Exactly how the presence of graphite, an effective solid lubricant material [73] decreases run-in is not evident, but may be related to interfacial and transfer film chemistry, or possibly more rapid polishing of the diamond surface, i.e. reduction of run-in by smoothing the film surface. In comparison, the correlation between total sp^2 content in the diamond films and run-in friction was not very strong. Based on the results here, the presence of nanocrystalline graphite, detectable as a trace amount in x-ray diffraction and by NEXAFS, appears to have a very beneficial effect on the tribological performance of these nanocrystalline diamond coatings.

6.2 Plasma and Materials Characteristics

The conditions needed for diamond deposition are creation of hydrocarbon radicals and ions to form the film and the correct ratio of species to promote growth rather than etching of the substrate.

Investigation of the reaction rate coefficients, as described in Chapter 4, for dominant second order methane reactions at the electron ion temperatures for each set of deposition conditions show that reaction mechanisms for the creation of CH_3^+ radicals and ions dominate. These are the preferred reactions for deposition of nanocrystalline diamond films.

Analysis of optical emission spectra to obtain plasma electron temperature for various gas mixing ratios has shown that once argon is added into the mixture, the plasma temperature changes. Pure hydrogen plasma has higher temperature (~ 5 eV) than a pure argon discharge (~ 1 eV). Adding hydrogen to the mixture of methane and argon increases the plasma temperature as shown in Figure 4.4.

Many neutral and ionization lines were seen in the UV and Visible spectra for the H36 plasma. All of these lines belong to either carbon or hydrogen containing molecules. One argon line was also identified in the spectra as shown in Figure 4.5. Spectral lines can be seen for neutral CH_x , with $x = 1, 2, 3,$ or 4 in the plasma. These are the sources of carbon for growth of the films.

7. Conclusions and Future Work

Nanocrystalline diamond coatings exhibited a low final friction coefficient <0.05 , and good wear resistance, i.e. surviving the test, for sliding against sapphire hemispheres. Their performance was correlated to their properties and structure, which were studied.

Plasma modeling and optical emission spectroscopy revealed plasma parameters, electron plasma temperature and number density, consistent with published results. Investigation of various reactions has shown the importance of dissociative mechanisms that produce CH_3 radicals and ions. Ions recombine while traveling towards the substrate and form radicals, which indicate the importance of abstraction reactions at the surface of the substrate. Future work would include developing a coupled plasma-surface deposition model that can predict and optimize the deposition of NCD.

Visible Raman spectra, XRD data, and NEXAFS spectra exhibit fingerprints for NCD films. Broad bands at 1350 and $1520\text{-}1580\text{ cm}^{-1}$ with shoulders at $1100\text{-}1150\text{ cm}^{-1}$ and $1430\text{-}1470\text{ cm}^{-1}$ and a shoulder at 1150 cm^{-1} are evident in the Raman spectra. These features are characteristic of NCD. The XRD analysis reveals small grain sizes, 5 to 10 nm, and changing film character. The order of sp^2 content varies with environment, as does the relative orientation of the diamond. Also, the general shape and peak location of the NEXAFS spectra discussed here are similar to characteristic NCD spectra in the literature. The NEXAFS data show distinct diamond character, but vary between 11 and 20 % sp^2 fraction. SEM and AFM image show that surface morphology and roughness vary with growth conditions.

In situ measurements of the contact diameter by direct measurement from video stills correlated well with *ex situ* profilometry measurements of counterface wear. For tests on coatings with evidence of graphite, wear of the sapphire counterface only occurred during the first 50 cycles or less followed by an interfacial sliding process between a carbonaceous transfer film and the wear track. The tribological performance of nanocrystalline diamond coatings was not influenced by coating roughness over the range studied (20 – 80 nm)

Friction run-in performance was influenced by coating chemistry and microstructure, a direct correlation between the amounts of graphite-structured sp^2 carbon in the NCD films (determined by both XRD and NEXAFS). Decreased run-in to low friction was observed. The shortest run-in times were attained for films containing the most graphite.

Coating wear was low and found to be polishing in nature. The surface morphology of as-prepared coatings smoothed quickly and the RMS track roughness decreased to below 10 nm during the first 100 sliding cycles.

Tribological performance of nanocrystalline diamond coatings was not influenced by coating roughness over the range studied (20 – 60 nm), whereas coating performance was influenced by coating chemistry. High friction run-in was minimized when there was a detectable graphitic peak in the x-ray diffraction. Run-in was also minimized with increasing sp^2 content.

The next steps in continuing this investigation are to continue with NCD deposition on the sapphire counterfaces. A process was developed for adhering NCD on the counterbodies, but more deposition of the variety of film coating conditions would allow for a wider range of testing. The characterization and tribology studies can be repeated with self-

mated NCD surfaces and compared to the sapphire on NCD results. Different results are likely since sapphire is a softer material than diamond and is subject to abrasion and wear by NCD coatings. Therefore, two identical surfaces being worn together may not exhibit the same friction and wear mechanisms. These NCD-NCD studies would give information useful to understanding mechanical systems on both the macro and micro scales.

8. References

- [1] R.D. McLellan, T. Biggerstaff, A.L. Winfrey, R.J. Nemanich, and G. Duscher, presented at the 211th Electrochemical Society Meeting, Chicago, IL, 2007 (unpublished)
- [2] D.M. Gruen, *Annu. Rev. Mater. Sci.* **29**, 211 (1999).
- [3] PW May, J.A. Smith, Yu. A. Mankelevich, *Diamond & Related Materials*, **15** 345 – 352 (2006).
- [4] Angus JC, Hayman CC. *Science*, 241, 913 (1988).
- [5] Michael Lieberman and Allan Lichtenberg, *Principles of Plasma Discharges and Materials Processing*, John Wiley & Sons, New York, 2nd Edition, pp. 495-497, 2005.
- [6] H. C. Shih, C. P. Sung, W. L. Fan, and W. L. Hsu, *Thin Solid Films* 232, 41 (1993).
- [7] W. Zhu, A. Inspektor, A. R. Badzian, T. Mckenna, and R. Messier, *J. Appl. Phys.* 68, 1489 (1990).
- [8] J. Reece Roth, *Industrial Plasma Engineering, Vol. 1: Principles*, Institute of Physics Publishing, Bristol, UK, pp. 468-492 , 1995.
- [9] Hideaki Yamada, Akiyoshi Chayahara and Yoshiaki Mokuno, “Simplified Description of Microwave Plasma Discharge for Chemical Vapor Deposition of Diamond”, *J. Appl. Physics*, Vol.101, 063302, 2007.
- [10] P.W. May, J.N. Harvey, J.A. Smith, and Y.A. Mankelevich, “Reevaluation of the mechanism of ultrananocrystalline diamond deposition from Ar/CH₄/H₂ gas mixtures, *Journal of Applied Physics* **99**, 104907 (2006).
- [11] Wu H-M., D.B. Graves, and R.K. Porteous, *Plasma Sources Science and Technology* (1994).

- [12] A.R. Krauss, O. Auciello, D.M. Gruen, A. Jayatissa, A. Sumant, J. Tucek, D.C. Mancini, N. Moldovan, A. Erdemir, D. Ersoy, M.N. Gardos, H.G. Busmann, E.M. Meyer, and M.Q. Ding, Ultrananocrystalline diamond thin films for MEMS and moving mechanical assembly devices, *Diamond and Related Materials* 10 (2001) 1952-1961
- [13] J.E. Gerbi, J. Birrell, M. Sardela, and J.A. Carlisle, Macrotecture and growth chemistry in ultrananocrystalline diamond thin films, *Thin Solid Films* 473 (2005) 41-48.
- [14] S. Jiao, A. Sumant, M. A. Kirk, D. M. Gruen, A. R. Krauss, and O. Auciello, Microstructure of ultrananocrystalline diamond films grown by microwave Ar-CH₄ plasma chemical vapor deposition with or without added H₂, *Journal of Applied Physics* 90 (2001) 118-122.
- [15] W. Kulisch and C. Popov, On the growth mechanisms of nanocrystalline diamond films, *Physica Status Solidi a-Applications and Materials Science* 203 (2006) 203-219.
- [16] Y. K. Liu, P. L. Tso, I. N. Lin, Y. Tzeng, and Y. C. Chen, Comparative study of nucleation processes for the growth of nanocrystalline diamond, *Diamond and Related Materials* 15 (2006) 234-238.
- [17] Y. C. Lee, S. J. Lin, D. Pradhan, and I. N. Lin, Improvement on the growth of ultrananocrystalline diamond by using pre-nucleation technique, *Diamond and Related Materials* 15 (2006) 353-356.
- [18] R. Ramamurti, V. Sharlov, R. N. Singh, S. Mamedov, and P. Boolchand, Raman spectroscopy study of the influence of processing conditions on the structure of polycrystalline diamond films, *Journal of Vacuum Science & Technology A* 24 (2006) 179-189.

- [19] D. Zhou, D.M. Gruen, L.C. Qin, T.G. McCauley, and A.R. Krauss, Control of diamond film microstructure by Ar additions to CH₄/H₂ microwave plasmas, *Journal of Applied Physics* 84 (1998) 1981-1989
- [20] A. Erdemir, G.R. Fenske, A.R. Krauss, D.M. Gruen, T. McCauley, and R.T. Csencsits, Tribological properties of nanocrystalline diamond films, *Surface and Coatings Technology*, 26th International Conference on Metallurgical Coatings and Thin Films, 12-15 April 1999 120-121 (1999) 565-572.
- [21] C. S. Abreu, F. J. Oliveira, M. Belmonte, A. J. S. Fernandes, J. R. Gomes, and R. F. Silva, CVD diamond coated silicon nitride self-mated systems: tribological behaviour under high loads, *Tribology Letters* 21 (2006) 141-151.
- [22] K. Holmberg and A. Matthews, *Coatings Tribology*, Elsevier, Amsterdam, 1994, p.51.
- [23] M. Godet, The third-body approach: a mechanical view of wear, *Wear* 100 (1984) 437-452.
- [24] I. L. Singer, S. D. Dvorak, K. J. Wahl, and T. W. Scharf, Role of third bodies in friction and wear of protective coatings, *Journal of Vacuum Science & Technology A (Vacuum, Surfaces and Films)* 21 (2003) S232-S240.
- [25] M. N. Gardos, Tribological fundamentals of polycrystalline diamond films, *Surface & Coatings Technology* 113 (1999) 183-200.
- [26] S.E. Grillo and J.E. Field, The polishing of diamond, *Journal of Physics D: Applied Physics* 30 (1997) 202-209.

- [27] S.E. Grillo, J.E. Field, and F.M. Van Bouwelen, Diamond polishing: the dependency of friction and wear on load and crystal orientation, *Journal of Physics D (Applied Physics)* 33 (2000) 985-990.
- [28] I.P. Hayward, I.L. Singer, and L.E. Seitzman, Effect of roughness on the friction of diamond on CVD diamond coatings, *Wear* 157 (1991) 215-227.
- [29] I. P. Hayward and I. L. Singer, The Tribological Behavior of Diamond Coatings, in: *New Diamond Science and Technology*, pp. 785-789, 1991.
- [30] I. P. Hayward, Friction and Wear Properties of Diamonds and Diamond Coatings, *Surface & Coatings Technology* 49 (1991) 554-559.
- [31] B. Bhushan, V.V. Subramaniam, A. Malshe, B.K. Gupta, and J. Ruan, Tribologically properties of polished diamond films, *Journal of Applied Physics* 74 (1993) 4174-4180.
- [32] S. J. Bull, P. R. Chalker, C. Johnston, and V. Moore, The Effect of Roughness on the Friction and Wear of Diamond Thin-Films, *Surface & Coatings Technology* 68 (1994) 603-610.
- [33] F.F. Chen, *Introduction to Plasma Physics and Controlled Fusion*, 2nd Ed., Plenum, New York (1984).
- [34] S.C. Brown, *Introduction to Electrical Discharges in Gasses*, John Wiley, New York (1966).
- [35] A.D. MacDonald, *Microwave Breakdown in Gasses*, John Wiley, New York (1966).
- [36] S. Praver and R. Nemanich, *Trans. R. Soc. Lond.* A362, 2537–2565, (2004).
- [37] R.J. Nemanich, J.T. Glass, G. Lucovsky, and R.E. Shroder, *J. Vac. Sci. Technol.* A6, 1783 (1988).

- [38] A.C. Ferrari and J. Robertson, *Phys. Rev. B* 63, 121405 (2001).
- [39] M. Park, A.T. Sowers, C. Lizzul Rinne, R. Schlessler, L. Bergman, R.J. Nemanich, Z. Sitar, J.J. Hren, and J.J. Cuomo, *J. Vac. Sci. Technol. B* 17.2., (1999).
- [40] R.J. Nemanich and S. A. Solin, *Phys. Rev. B* 20, 392 (1979).
- [41] A. Richter, H.-J. Scheibe, W. Pompe, K.-W. Brzezinka, and I. Mühling, *J. Non-Cryst. Solids* 88, 131 (1986).
- [42] S. Praver, K. W. Nugent, Y. Lifshitz, G. D. Lempert, E. Grossman, J. Kulik, I. Avigal, and R. Kalish, *Diamond Relat. Mater.* 5, 433 (1996).
- [43] A.C. Ferrari and J. Robertson, Origin of the 1150 cm⁻¹ Raman mode in nanocrystalline diamond, *Physical Review B (Condensed Matter and Materials Physics)* 63 (2001) 121405-121401.
- [44] R. J. Nemanich, J. T. Glass, G. Lucovsky, and R. E. Shroder, Raman-Scattering Characterization of Carbon Bonding in Diamond and Diamondlike Thin-Films, *Journal of Vacuum Science & Technology A* 6 (1988) 1783-1787.
- [45] S. Praver and R.J. Nemanich, Raman spectroscopy of diamond and doped diamond, *Philosophical Transactions of the Royal Society London, Series A (Mathematical, Physical and Engineering Sciences)* 362 (2004) 2537-2565.
- [46] J. Birrell, J.E. Gerbi, O. Auciello, J.M. Gibson, J. Johnson, and J.A. Carlisle, Interpretation of the Raman spectra of ultrananocrystalline diamond, *Diamond and Related Materials* 14 (2005) 86-92.
- [47] A. C. Ferrari and J. Robertson, Resonant Raman spectroscopy of disordered, amorphous, and diamondlike carbon, *Physical Review B* 64 (2001).

- [48] H.P. Klug, X-ray diffraction procedures for polycrystalline and amorphous materials, Wiley, New York, 1974, pp.661-665.
- [49] G. K. Williamson and W. H. Hall, X-Ray Line Broadening from Filled Aluminium and Wolfram, *Acta Metallurgica* 1 (1953) 22-31.
- [50] P. K. Bachmann, H. D. Bausen, H. Lade, D. Leers, D. U. Wiechert, N. Herres, R. Kohl, and P. Koidl, Raman and X-Ray Studies of Polycrystalline CVD Diamond Films, *Diamond and Related Materials* 3 (1994) 1308-1314.
- [51] L. Fayette, M. Mermoux, B. Marcus, F. Brunet, P. Germi, M. Pernet, L. Abello, G. Lucazeau, and J. Garden, Analysis of the Fine-Structure of the Raman Line and of X-Ray Reflection Profiles for Textured Cvd Diamond Films, *Diamond and Related Materials* 4 (1995) 1243-1250.
- [52] L. Fayette, B. Marcus, M. Mermoux, G. Tourillon, K. Laffon, P. Parent, and F. Le Normand, Local order in CVD diamond films: Comparative Raman, x-ray-diffraction, and x-ray-absorption near-edge studies, *Physical Review B* 57 (1998) 14123-14132.
- [53] F. Silva, F. Benedic, P. Bruno, and A. Gicquel, Formation of $\langle 110 \rangle$ texture during nanocrystalline diamond growth: an X-ray diffraction study, *Diamond and Related Materials* 14 (2005) 398-403.
- [54] Y. Ufuktepe, G. Akgul, and J. Luning, X-ray photoabsorption and total electron yield of Fe thin films at the L-2,L-3 edge, *Journal of Alloys and Compounds* 401 (2005) 193-196.
- [55] M. Jaouen, G. Tourillon, J. Delafond, N. Junqua, and G. Hug, A Nexafs Characterization of Ion-Beam-Assisted Carbon-Sputtered Thin-Films, *Diamond and Related Materials* 4 (1995) 200-206.

- [56] C. Lenardi, M. A. Baker, V. Briois, L. Nobili, P. Piseri, and W. Gissler, Properties of amorphous a-CH(: N) films synthesized by direct ion beam deposition and plasma-assisted chemical vapour deposition, *Diamond and Related Materials* 8 (1999) 595-600.
- [57] R. Gago, I. Jimenez, and J. M. Albella, Detecting with X-ray absorption spectroscopy the modifications of the bonding structure of graphitic carbon by amorphisation, hydrogenation and nitrogenation, *Surface Science* 482 (2001) 530-536.
- [58] I. Jimenez, R. Gago, J. M. Albella, D. Caceres, and I. Vergara, Spectroscopy of pi bonding in hard graphitic carbon nitride films: Superstructure of basal planes and hardening mechanisms, *Physical Review B* 62 (2000) 4261-4264.
- [59] R. J. Nemanich and S. A. Solin, 1st-Order and 2nd-Order Raman-Scattering from Finite-Size Crystals of Graphite, *Physical Review B* 20 (1979) 392-401.
- [60] James Birrell, J.E. Gerbi, O. Auciello, J.M. Gibson, J. Johnson, J.A. Carlisle, *Diamond & Related Materials* 14, 86– 92 (2005).
- [61] B. Rothman, Technical Report on Hydrogen Concentration, (2006).
- [62] A. von Engel, *Electric Plasmas: their nature & uses*, International Publication Service, Taylor & Francis Inc., New York, pp.123-125, (1983).
- [63] H. Griem, *Plasma Spectroscopy*, McGraw-Hill, New York (1964).
- [64] M. Bauer, T. Schwarz-Selinger, H. Kang, and A. von Keudell, Controll of the plasma chemistry of a pulsed inductively coupled methane plasma, *Plasma Sources Science and Technology*, 14 543-548 (2005).

- [65] T. W. Scharf and I. L. Singer, Role of third bodies in friction behavior of diamond-like nanocomposite coatings studied by *in situ* tribometry, *Tribology Transactions* 45 (2002) 363-371.
- [66] R.R. Chromik, A.L. Winfrey, R.J. Nemanich, and K.J. Wahl, Run-in behavior of nanocrystalline diamond coatings studied by *in situ* tribometry, accepted to *Wear* (2007).
- [67] E. P. Whitemton and P. J. Blau, A Comparison of Methods for Determining Wear Volumes and Surface Parameters of Spherically Tipped Sliders, *Wear* 124 (1988) 291-309.
- [68] I.L. Singer, Solid Lubrication Processes, in: I.L. Singer and H.M. Pollock, *Fundamentals of Friction: Macroscopic and Microscopic Processes*, Netherlands, pp. 237-261, 1992.
- [69] K.J. Wahl and I.L. Singer, Quantification of a lubricant transfer process that enhances the sliding life of a MoS₂ contact, *Tribology Letters* 1 (1995) 59.
- [70] Y. Enomoto and D. Tabor, The Frictional Anisotropy of Diamond, *Proceedings of the Royal Society of London Series a-Mathematical Physical and Engineering Sciences* 373 (1981) 405-417.
- [71] J.R. Hird and J.E. Field, Diamond polishing, *Proceedings of the Royal Society of London, Series A (Mathematical, Physical and Engineering Sciences)* 460 (2004) 3547-3568.
- [72] R. McCann, S. S. Roy, P. Papakonstantinou, M. F. Bain, H. S. Gamble, and J. A. McLaughlin, Chemical bonding modifications of tetrahedral amorphous carbon and nitrogenated tetrahedral amorphous carbon films induced by rapid thermal annealing, *Thin Solid Films* 482 (2005) 34-40.
- [73] F.P. Bowden and D. Tabor, *The friction and lubrication of solids*, Clarendon, Oxford, 1986.